Mapping Diffusion in Complex Media

Characterizing a Single Plane Illumination Microscope for Imaging Fluorescence Correlation Spectroscopy

By M. Ahmad Mahmood,

A Thesis Submitted to the School of Graduate Studies in Partial Fulfillment of the Requirements for the Degree of Master of Science

McMaster University

Master of Science (2020)

Hamilton, Ontario (Department of Physics and Astronomy)

TITLE: Characterizing a Single Plane Illumination Microscope for Imaging Fluorescence Correlation Spectroscopy

AUTHOR: M. Ahmad Mahmood (McMaster University)

SUPERVISOR: Dr. Cécile Fradin

NUMBER OF PAGES: xv, 92

Abstract

In many systems, *in vitro* or *in vivo*, it has become important to experimentally obtain dynamical information at many different positions simultaneously. This is a challenge as conventionally, dynamic information in biological systems is probed with a confocal microscope to perform either fluorescence correlation spectroscopy (FCS) or fluorescence recovery after photobleaching (FRAP), which can be damaging due to phototoxicity, and yields information at a single position. Advances in camera sensors have allowed their use in place of single point detectors and the implement of imaging FCS by way of single plane illumination microscopy (SPIM). In this modality, a light sheet with a thickness of only a few microns illuminates the sample and the fluorescence is projected orthogonally onto the camera chip. By imaging small regions of interest at a very high frame rate, we can determine dynamic parameters such as diffusion coefficients and local concentrations in a 2D array of pixels. In this thesis, I discuss the theoretical background, hardware setup, design and characterization of a SPIM which I have built in order to perform imaging FCS.

Acknowledgements

This thesis would not have been possible if not for the love and support of my family and friends. This work, and any work I have done in the past, and hope to do in the future, is dedicated to my parents. They uprooted their lives and moved across the world so that their children could pursue their passions, and I was lucky enough to find something that I love doing so much.

My passion for biophysics was inspired by Dr. Cécile Fradin, who gave me a chance as an undergraduate student to work in her lab. The greatest skill she has taught me is how to think critically, which is something I will take with me for the rest of my career. I have had the privilege of travelling across Canada, and the world, to further my education in biophysics, and none of it would have been possible without her generosity. Her kindness and compassionate nature towards students is something I hope to emulate. Without a doubt, she has shaped me into the scientist I am today.

My research experience would have not been as enjoyable if not for the graduate students and undergraduates who've I've had the pleasure of working with over the last 4 years in the Fradin Lab. Carmina, Michael, and Markus all had such a wealth of knowledge, and their help in fruit fly care, optics, and wet lab skills respectively is invaluable. Lili has been such a help over the last year since she's joined the lab, and I trust her to take the light sheet to new levels. This list wouldn't be complete without Liu, who has made coming to work such a fun experience, and the one thing I'll miss the most is working out together. I would also like the thank the many graduate students outside the lab in the Department of Physics and Astronomy who made my experience as a graduate student so much more enjoyable, especially Carmen and Erica. I would also like to thank Dr. Thorsten Wohland and Fereydoon Taheri for their insight into SPIM-FCS.

I'd like to thank my amazing friends outside of work who kept me grounded over the last few years. Aimee and Jaclyn, you two have been my rock and always will be. Abbey, Sam, and Julia, I didn't think I'd make lifelong friends when I started undergrad, but I am so happy I did. Batool, Simren, Ramya, Tanya, and Kimberly, your friendships mean the world to me. Lastly, to Jesse and Haddon 15, for making this last year the most amazing.

Contents

List of Figures

List of Tables

Declaration of Authorship

I, M. Ahmad Mahmood, declare that this thesis titled, "Characterizing a Single Plane Illumination Microscope for Imaging Fluorescence Correlation Spectroscopy" and the work presented in it are my own. I confirm that the following listed work is my own:

Part 1 - Introduction

- Diffusion
  - Background information summarized from various texts on diffusion processes and how diffusion is studied through confocal fluorescence correlation spectroscopy.
- Mathematical Formalism for SPIM-FCS
  - Mathematical formulae summarized from notable texts regarding the theory behind SPIM-FCS and functions to model single component diffusion.

Part 2 - SPIM-FCS: Development and Instrumentation

- SPIM-FCS Hardware
  - The hardware, including optical components, and design choices made to build a SPIM-FCS.
  - Focus on data analysis.
  - Experimental results that show the physical characteristics of the light sheet.

Part 3 - SPIM-FCS: Results

- Characterizing Bead Diffusion in Solution
  - Post processing of ACF curves.
  - Calibration of lateral point spread function.
  - Absolute diffusion coefficients and concentrations of 100 nm bead samples.
- Imaging Nuclei in *D. melanogaster*
  - Imaging capabilities of the SPIM on fluorescently labelled fly embryos.

Part 4 - Conclusion

- Conclusion
  - Final remarks about the results obtained from the SPIM-FCS.
  - Future alterations that can be made to better the SPIM-FCS instrument.

Part I

Introduction

Aim of the thesis

The goal of my project was to build an instrument to combine two optical techniques: single plane illumination microscopy (SPIM) and imaging fluorescence correlation spectroscopy. This method, known as SPIM-FCS, was established by Wohland et al. 2010. SPIM allows the illumination of complex and thick samples, such as embryos, with a two-dimensional sheet of light with finite thickness providing fast optical sectioning of these samples. The light from the illuminated slice of the sample is captured using an orthogonal detection scheme. The sample is imaged with a sensitive high speed camera (sCMOS) over a small field of view (FOV) where each pixel now acts as a confocal FCS volume. This is the method of imaging FCS. A schematic of a SPIM-FCS instrument is shown in Figure 1. This technique can be used to obtain diffusion coefficient from each pixel in the FOV, allowing to construct a 2D diffusion map for each slice in the sample. The SPIM-FCS built was used to characterize diffusing beads in solution as a way to demonstrate the viability of this instrument to accurately measure diffusion coefficients and concentrations.

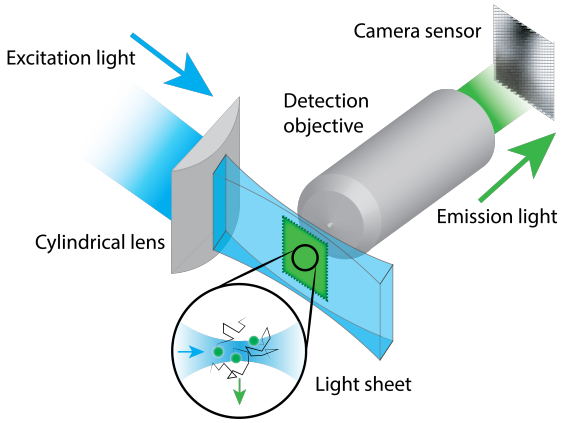

FIGURE 1: Simplified schematic of a SPIM-FCS instrument. The excitation/illumination light is shaped by a cylindrical lens into a sheet of light with finite thickness. The light sheet interacts with a fluorescent sample. The emission/fluorescent light is captured by a detection objective orthogonal to the path of the illumination light. The fluorescent light is detected on a camera chip.

Thesis structure

In Part I Chapter 1, I will give a brief overview of diffusion mechanisms and how they are studied experimentally though fluorescent labelling and FCS. I will continue in Chapter 2 to rigorously define the mathematical formulae used to describe fluorescence fluctuation methods that pertain to both confocal and SPIM-FCS. In Part II, Chapter 3 will discuss in depth the hardware development of a home built SPIM-FCS and the experimentally determined characteristics of the system. I will conclude in Part III by demonstrating the capabilities of the SPIM-FCS instrument in accurately measuring concentrations and absolute diffusion coefficients, as well as its *in vivo* imaging ability.

Chapter 1

Diffusion

1.1 Diffusion processes

In 1827 while looking at pollen grains in water under a light microscope, Robert Brown observed the erratic motion of the sub micron lipid particles contained in the pollen, which moved in a seemingly random pattern (Brown 1828). Later, in 1905, Albert Einstein published a paper describing the motion that Brown observed as the result of collisions between the water molecules and the lipid particles (Einstein 1905). Einstein's predictions were experimentally verified by Jean Perrin in 1908 earning him a Nobel Prize in Physics in 1926 for his work on the discontinuous nature of matter, i.e. the existence of molecules and atoms (Perrin 1910).

1.1.1 Brownian motion

Brownian motion is a random walk resulting in a diffusive process, where it is equally likely to move in any direction and each step is independent of the previous one. Einstein's theory for Brownian motions involved the formalization of the diffusion equation, shown for 1D diffusion in Equation 1.1, where ρ represents the concentration of the

diffusing molecules at a given point in space and time:

$$\frac{\partial \rho}{\partial t} = D \cdot \frac{\partial^2 \rho}{\partial x^2}, \tag{1.1}$$

where D is the diffusion coefficient which is related to the mean squared displacement of the particle undergoing Brownian motion. The solution to this PDE, for particles initially placed at $x = 0$ is given by Equation 1.2:

$$\rho(x,t) = \frac{N}{\sqrt{4\pi D t}} \cdot e^{\frac{-x^2}{4Dt}}, \tag{1.2}$$

where N is the number of particles starting at the origin at $t = 0$. This is a Gaussian distribution and it has a characteristic bell shape. At $t = 0$, ρ is a Dirac delta distribution as all particles are located at the origin. As $t \to \infty$ the distribution flattens out and becomes uniform. This is shown in the 2D plot in Figure 1.1

The diffusion coefficient D is related to how fast this distribution flattens and spreads. If the particles are moving faster, the diffusion coefficient is higher. On the other hand, the more viscous the material they move in and the larger they are, the slower the particles move, and the smaller their diffusion coefficient. By relating this to the thermal unit of energy $k_B \cdot T$:

$$D \propto \frac{k_B T}{\eta \cdot R}, \tag{1.3}$$

where k_B, T, η, R are the Boltzmann constant, temperature, viscosity, and hydrodynamic radius respectively. Approximating the particle to a sphere, its Stokes drag is

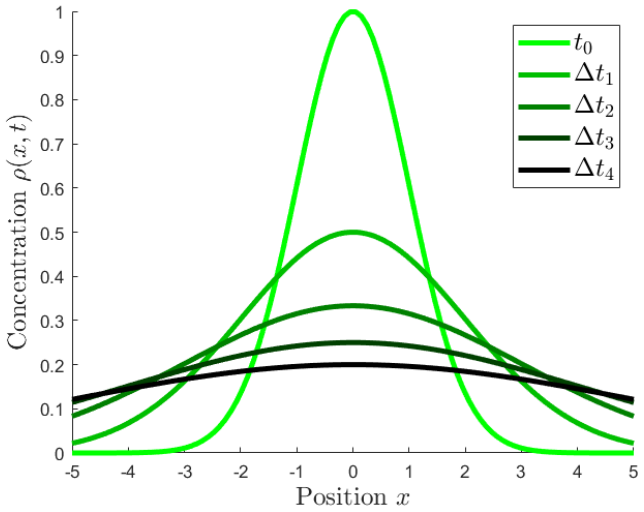

FIGURE 1.1: Two dimensional spread over time of particles undergoing Brownian motion. The bright green curve indicated by t_0 shows the spatial distribution along one direction (here, the x axis) of particles at $t = 0$. As $t \to \infty$, which is indicated in the plot as the curves darken to black, the distribution approaches a flat line indicating a uniform distribution across space.

given by $6\pi \cdot \eta R$, leading to the Stokes-Einstein relationship:

$$D = \frac{k_B T}{6\pi\eta \cdot R}. \tag{1.4}$$

Now, to establish the relationship between the diffusion coefficient and the mean squared displacement, we calculate the first and second moments of Equation 1.2. The first moments in both dimensions are (integrating over all space, and turning Equation 1.2 into two dimensions):

$$\langle x \rangle = \langle y \rangle = \int_{-\infty}^{\infty} x \cdot \rho(x, y, t)\, \mathrm{d}x = \int_{-\infty}^{\infty} y \cdot \rho(x, y, t)\, \mathrm{d}y = 0. \tag{1.5}$$

The second moment is given by (using polar coordinates):

$$\langle r^2 \rangle = \int_0^{2\pi} \int_{-\infty}^{0} r^2 \cdot \rho(x, y, t) \cdot r \, \mathrm{d}r\mathrm{d}\theta = 4Dt \tag{1.6}$$

This is the mean squared displacement (MSD) in two dimension. For n dimensions:

$$\langle r^2 \rangle = 2nDt. \tag{1.7}$$

With the Stokes-Einstein relationship 1.4, and by rearranging for t in Equation 1.7, we can estimate the time it takes for a particle undergoing Brownian motion to traverse an object of distance L.

$$t = \frac{L^2}{2nD} \overset{n=3}{=} \frac{L^2}{6D} \tag{1.8}$$

The following are back-of-the-envelope calculations obtained from the book *Cell Biology by the Numbers* by Milo and Phillips (Orme et al. 2016).

TABLE 1.1: Diffusion time scales of a 30 kDa protein with diffusion coefficient $10\mu m^2/s$ moving inside cells of varying length scales

Cell	Length	Characteristic time t
E. coli	1 μm	$\approx$10 ms
HeLa cell	20 μm	$\approx$10 s
Neuronal Cell Axon	1 cm	$\approx 10^6$ s = 10 days

The above examples assume a perfectly diffusing free Brownian particle. The hallmark of such a diffusing particle is the fact that the MSD in Equation 1.7 has a linear dependence on time t. In the following section, I'll discuss deviations from this linearity.

1.1.2 Anomalous diffusion

In a cell, the physical environment is very crowded with macromolecules such as other proteins, or larger subcellular complexes. These crowded environments can have a large effect on the thermodynamic activity within the cells which largely influences diffusion (Zimmerman and Trach 1991). Due to the presence of other macromolecules in high concentration, large volumes within the cell are inaccessible to the diffusing particles. If the fraction of space that is inaccessible is large enough, the random nature of Brownian motion is affected. In this case the MSD is no longer a linear function of time as described in Equation 1.7, but instead can often be described by a power-law (Höfling and Franosch 2013,Weiss et al. 2003):

$$\langle r^2 \rangle = 2d \cdot \Gamma \cdot t^{\alpha}; \;\; 0 < \alpha < 1. \tag{1.9}$$

In the above equation, α is the anomaly exponent, and Γ is the generalized diffusion coefficient, whose units depend on α, $[\Gamma] = m^2/s^{\alpha}$.

What Equation 1.9 shows is that the diffusion is not only slower in cases of crowded environments, but the trajectory of particles is also greatly affected. In Figure 1.2, we see the linear nature of normal diffusion, and the deviations from this linear behaviour as subdiffusion with $\alpha < 1$ and superdiffusion when $\alpha > 1$. The latter is not discussed in this thesis, but is encountered in cells for large particles (100 nm to a few μm) whose diffusion isn't fast enough, so it must be facilitated by other proteins and complexes.

1.2 Measuring diffusion in living organisms

The experimental methods that are used for determining the diffusion coefficients of biological molecules involves the fluorescent tagging of these molecules so that they can

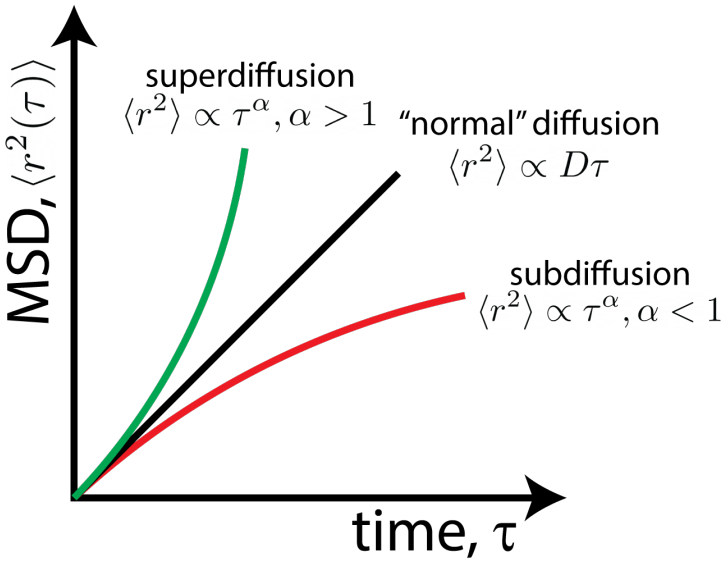

FIGURE 1.2: MSD of particles undergoing varying transport methods.

be differentiated from their host environment. Here, I will spend some time discussing the concept of fluorescence, and how it is applied to the study of living systems.

1.2.1 Fluorescence mechanisms

This subsection provides a brief overview of the mechanisms by which molecules can emit light. Much of the information is provided by Lakowicz 2006, a great resource for further information. Luminescence is the process by which a molecule will be excited by a photon of a certain energy, and emit a photon at a lower energy. This can be subdivided into two processes, fluorescence and phosphorescence, which is dependent on the nature of the excited state. A molecule that can fluoresce is known as a flurophore. When the fluorophore is in the ground state, electrons of opposite spin occupy this ground state. When one of the valence electrons gets excited by a photon, it usually is excited to a higher state while conserving its spin. These are known as singlet ground state and single excited states, respectively. Relaxation from a singlet excited state is known as fluorescence and has an excited lifetime in the range of nanoseconds (Figure 1.3). However, while in the excited state, there is a small probability for excited valence

electrons to flip their spin so that it matches the spin of their pair ground state electron. The resulting state is known as a triplet state and occurs through intersystem crossing (shown in Figure 1.4). The name "triplet" comes from the calculation of multiplicity of the energy level in the excited state, which is a measure of the possible orientations of the spin. If we look at Figure 1.3 **C.**, the multiplicity is calculated by $2(S)+1$, where S is the sum of all the electron spins. Thus, the multiplicity is $2(1/2+1/2)+1=3$, giving the title triplet state. Relaxation from the triplet state is known as phosphorescence and has an excited lifetime in the range of microseconds to many minutes (Figure 1.3).

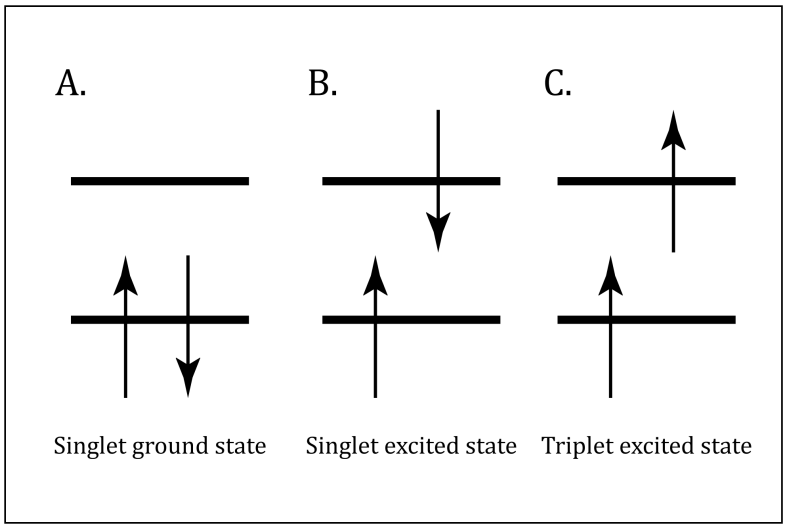

FIGURE 1.3: **A.** Singlet ground state of a fluorophore displaying the opposite spin pair electrons in the valence shell. **B.** After excitation by a photon, one electron in the singlet pair is now in a higher energy level while conserving spin. **C.** After excitation by a photon, one electron in the singlet pair is now in a higher energy level while the spin is flipped to match that of the electron in the ground state. This state is known as the triplet excited state.

When a photon is absorbed by a fluorophore, the electronic state of the molecule is moved from the ground state S_0 to the first excited state S_1 (or higher, but for simplicity we'll assume it goes to S_1). We will also assume here that it goes into an excited singlet state. This excitation is a type of radiative transfer, where the electron has interacted with a photon. When a molecule is excited, not only is the electronic configuration

altered, but also the nuclear configuration. This is described by the Franck-Condon principle which stems from the fact that the nuclear mass (consisting of neutrons and protons) is much larger than the electronic mass. When an electron experiences an energy transition, the timescale is so fast (on the order of nanoseconds) that the nuclear mass remains unperturbed. However, the altered electronic configuration causes a delayed change in the Coulombic forces on the nuclei which results in a change in the vibrational state of the molecule. These vibrational states are quantized and have energy levels much closer to one another than electronic configurations (Gupta 2016). Non radiative transitions occur in the sub electronic energy levels of an excited state where electronic energy is converted to vibrational energy which results in the occupation of a lower excited state. This is known as internal conversion. This increase in vibrational energy is dissipated into the surrounding medium as heat. This loss in energy causes the radiative transfer from the singlet excited state to the ground state to have lower energy, and thus longer wavelength compared to the excitation photon. This is seen as a shift in the excitation/emission spectrum of the fluorophore which is called the Stokes shift. This is shown graphically below in the form of a Jablonski diagram in Figure 1.4. The Stokes shift is important in discerning between the light used to excite fluorophores versus the light that is emitted.

Fluorescent proteins (FP) and other fluorescent molecules

There are different types of fluorescent molecules that can be used in experiments, and which one is best will depend entirely on the application. FPs (mutants or other derivatives) are proteins derived from aquatic life. The most famous of these is the green fluorescent protein (GFP) derived from the jellyfish (Shimomura 1979). The gene coding for GFP can be expressed in other living organisms using recombinant complementary DNA cloning technology. This gene is then translated to produce GFP in the organism, which is then fluorescent under light excitation. This allows the tracking and visualization of

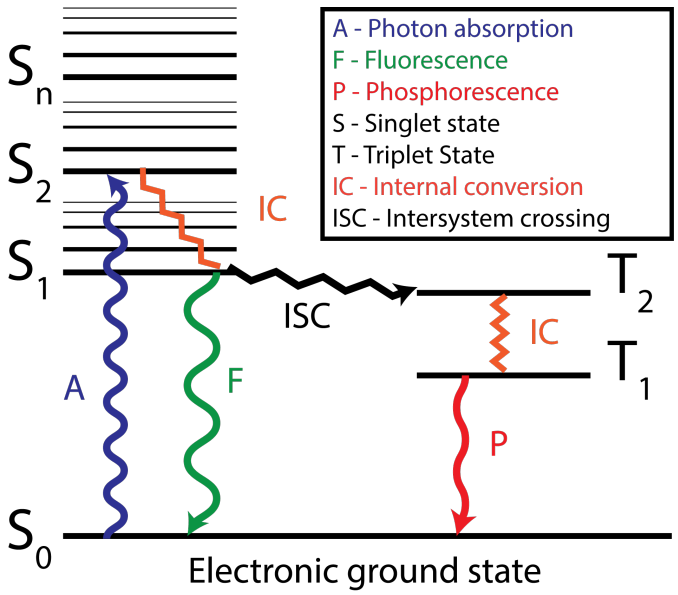

FIGURE 1.4: This is a Jablonski diagram. This graphically describes the process of photon absorption by a fluorophore, and the electronic state changes that occur which lead to fluorescence and phosphorescence.

molecules *in vivo*. Other useful fluorescent molecules include cyanine dyes which are synthetic dyes characterized by their aromatic rings. They are very photostable, and have a high quantum yield. (Shindy 2017). Quantum dots, unlike cyanine dyes and GFP which are organic molecules, are nanometer sized semiconductors. Their mechanism of fluorescence is much different in that the excitation photon creates an electron-hole pair. The recombination of the electron hole pair results in the emission of a photon of lower energy. The energy of the emitted light is dependent on the size of the nanocrystal. Small variances on the order of $1/10^{th}$ of a nanometer can result in different wavelengths (Chakraborty and Apalkov 2003).

In this thesis, fluorescent polystyrene microspheres (0.1 ± 0.0072 μm in diameter) from Thermo Fisher Scientific labelled with proprietary dye (with an equivalent of 74000 Fluorescein molecules per bead) were used to characterize the SPIM-FCS instrument. They were chosen due to their photostability and monodisperse size distribution allowing for accurate characterization. To test the imaging capabilities of the SPIM, enhanced

GFP (eGFP) labelled Bicoid protein that is expressed in *Drosophila melanogaster* was used.

1.2.2 Fluorescence correlation spectroscopy: Principle

There exist several subgroups of fluorescence techniques that can help measure the diffusion of particles, for example single particle tracking where each diffusing particle must be adequately resolved (Manzo and Garcia-Parajo 2015), or intensity fluctuation methods where statistical information about the particles is collected and analyzed (Rigler et al. 1993). For the purpose of this thesis, I will focus on the latter.

Here I describe the general principle of correlation spectroscopy and derive the general expressions for the fluorescence signal detected in an FCS experiment and the autocorrelation function (ACF) used in this type of experiment. The following formalism is discussed in greater depth in Chapter 2 for specific experimental geometries and samples, as well as in Krichevsky and Bonnet 2002.

If we consider that we have a solution containing m different non-interacting species, then, each species k has a local concentration of $c_k(\vec{r},t)$ and a global average concentration of $\langle c_k(\vec{r})\rangle_t$. At equilibrium, the system does not change, however, if the system is observed over a short timescale, and over a small fraction of the volume, fluctuations around the average concentration can be observed:

$$c_k(\vec{r},t) = \langle c_k(\vec{r})\rangle_t + \delta c_k(\vec{r},t). \tag{1.10}$$

The distribution of the excitation light in the sample is denoted by $I(\vec{r})$. By assuming that the number of photons collected from each fluorescing molecule is proportional to

the sampling time Δt, the number of photons collected over Δt is:

$$n(t) = \Delta t \int d^3\vec{r}\ I(\vec{r}) \sum_{k=1}^{m} \eta_k c_k(\vec{r}, t), \tag{1.11}$$

where η_k describes the product of the absorption cross section by the fluorescence quantum yield and the efficiency of fluorescence detection for the component k. Then, the fluctuation of the intensity, $\delta n(t)$, around the mean, $\bar{n} = \langle n(\vec{t}) \rangle$ is,

$$\delta n(t) = n(t) - \bar{n} = \Delta t \int d^3\vec{r}\ I(\vec{r}) \sum_{k=1}^{m} \eta_k \delta c_k(\vec{r}, t) \tag{1.12}$$

The dynamics of the system is encoded into the fluctuations in the intensity of the fluorescent particles. To extract this information, the intensity fluctuations are compared to themselves over logarithmic timescales. This process is known as autocorrelation, and generates the autocorrelation function (ACF), $G(\tau)$:

$$G(\tau) = \frac{1}{\bar{n}^2 T} \sum_{i=0}^{T-1} \delta n(t) \delta n(t + \tau). \tag{1.13}$$

Here, T denotes the total number of sampling intervals such that $\Delta t \cdot T$ is the total duration of the experiment. The lag time τ represents the time between which the intensity trace is compared to itself. Autocorrelation functions are usually calculated using commercially bought correlators directly connected to the photon detector allowing to quickly obtain correlation functions over a logarithmic timescale, which can extend down to 10-100 ns.

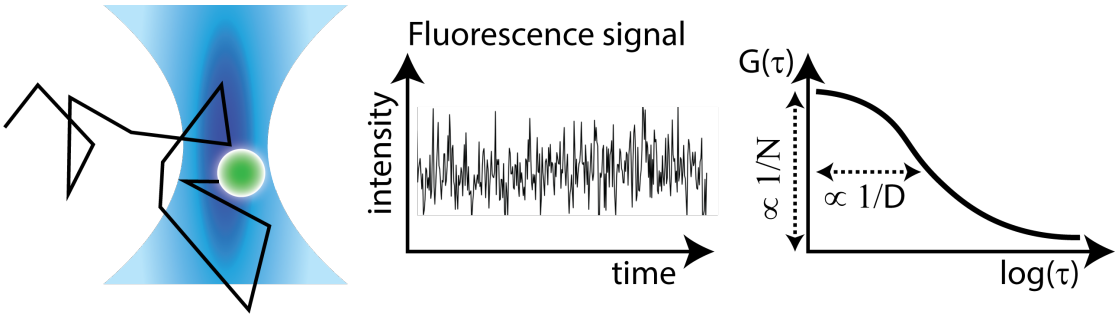

FIGURE 1.5: The intensity trace of a fluorescent molecule undergoing Brownian motion in an excitation volume. The trace is autocorrelated to obtain the ACF to extract dynamical parameters.

1.2.3 FCS: Confocal instrumentation

Classically, FCS is performed using an inverted confocal setup. In this modality, one uses a pinhole to reject the out of focus light that hits the detector to remove any background out of focus fluorescence. The intensity profile described in Equation 1.11 is not just the excitation intensity profile, but the excitation multiplied by the detection efficiency to take into account the shape of the pinhole. The excitation volume is very small, on the order of femtoliters roughly the shape of a prolate ellipsoid, with a diffraction-limited radius of $w_{xy} \approx 250$ nm, so it is referred to as "a point". This provides the small subvolume required to detect 10 to 100 particles at concentrations in the nM range (Rigler et al. 1993). Such a focal volume is shown in Figures 1.5 and 1.6.

The intensity profile (multipled by the detection efficiency) of a confocal laser beam at the focus can be modelled by a Gaussian illumination intensity profile as seen in Equation 1.14

$$I(\vec{r}) = I_0 \cdot \exp\left(-\frac{2(x^2+y^2)}{w_{xy}^2} - \frac{2z^2}{w_z^2}\right) \tag{1.14}$$

where w_z and w_{xy} denote the beam $1/e^2$ radius in the direction of the propagation of light and in the focal plane, respectively. More complex models exist that describe

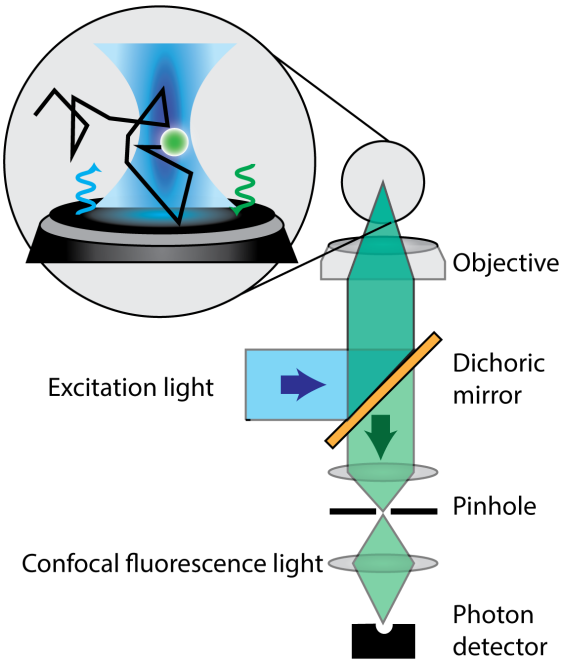

FIGURE 1.6: A confocal setup for performing FCS.

the intensity profile more accurately, such as the use of a Lorentzian function in the z direction (Rigler et al. 1993). Using these geometric parameters for the illumination, analytical models can be created to fit the ACFs. These models are specific to the type of diffusion expected. For example, as we will see in Chapter 2, for single component diffusion,

$$G(\tau) = \frac{1}{\bar{N}}\left(1+\frac{1}{\tau_D}\right)^{-1}\left(1+\frac{1}{\omega^2\tau_D}\right)^{-1/2} \tag{1.15}$$

where $\bar{N} = V\langle c\rangle$, $V = \pi^{3/2}w_{xy}^2 w_z$ is the excitation volume, and $\langle c\rangle$ is the average concentration, thus $\bar{N}$ is the average number of molecules within the excitation volume. $\tau_D = w_{xy}^2/4D$ represents the characteristic diffusion time across the illumination volume. Derivation of Equation 1.15 and additional expressions for different diffusion models can be found in Krichevsky and Bonnet 2002. In 2, an equivalent expression will derived for SPIM-FCS (ie. for a light sheet, instead of a confocal, illumination).

1.2.4 FCS: *in vivo*

An interesting biological system to study from the perspective of diffusion is the formation of morphogen gradients which dictate the structural formation of fly embryos during early embryogenesis. Previous studies done by Abu-Arish et al. 2010, have shown that the diffusion coefficient and the concentration of Bicoid could be measured in live fly embryos using confocal fluorescence correlation spectroscopy (FCS), and that this diffusion coefficient 7 $\mu m^2/s$ was large enough to explain how Bicoid could form a concentration gradient over the full 500 μm length of the embryo in less than 1 hr (Abu-Arish et al. 2010). Morphogen gradient formation was studied in zebrafish embryos by Yu et al. 2009 by FCS. They determined that Fgf8 gradient formation can be explained by normal diffusion of molecules away from the source, and a sink function of the receiving cells, mediated by receptor-mediated endocytosis.Korzh et al. 2008 studied the development of the liver in zebrafish embryos by measuring the blood flow using FCS. They determined that blood circulation is critical in maintaining the vascular network to support liver growth. However, experiments performed using confocal FCS only provide diffusion coefficients at singular points within the three-dimensional embryo, which is a very heterogeneous environment. Furthermore, due to the method of illumination, large portions of the live sample are photobleached, leading to a decay in the intensity trace over time which dramatically influences ACFs generated. Image correlation spectroscopy by raster scanning was done by Digman and Gratton 2009 to study the transient binding of macromolecules and semi-immobile structures within the cytoplasm of cells. This imaging spectroscopy method was able to determine this weakly binding interaction and diffusion process. All these great pieces of research point to the fact that if the system is heterogeneous, single point FCS only provides a limited picture of the internal dynamics of the molecules of interest. As such, by way of imaging FCS, one is able to multiplex the FCS system, and gain spatial insight inside complex systems.

Chapter 2

Mathematical Formalism for SPIM-FCS

This chapter will provide the derivation of mathematical models that analytically describe fluorescence fluctuations in a SPIM FCS system to extract meaningful physical parameters such as absolute diffusion coefficients and concentrations. It will provide the fundamental understanding of how camera based detection (as opposed to single point detection as used in confocal FCS) influences the shape of the ACF. This chapter builds on Section 1.2.2, where the ACF expected for simple diffusion in single point FCS was defined. This formalism is adapted from Born and Wolf 1999, Lasser and Hassler 2005, Rigler et al. 1993, and Wolfgang Krieger 2014.

2.1 Molecular Detection Efficiency

We start by using Figure 2.1 to illustrate a general fluorescence excitation and detection setup that can used for FCS experiments. This general formalism assumes a single species, a single excitation laser line, and a single detection channel.

A laser beam is focused by illumination optics that are unique to the microscope setup,

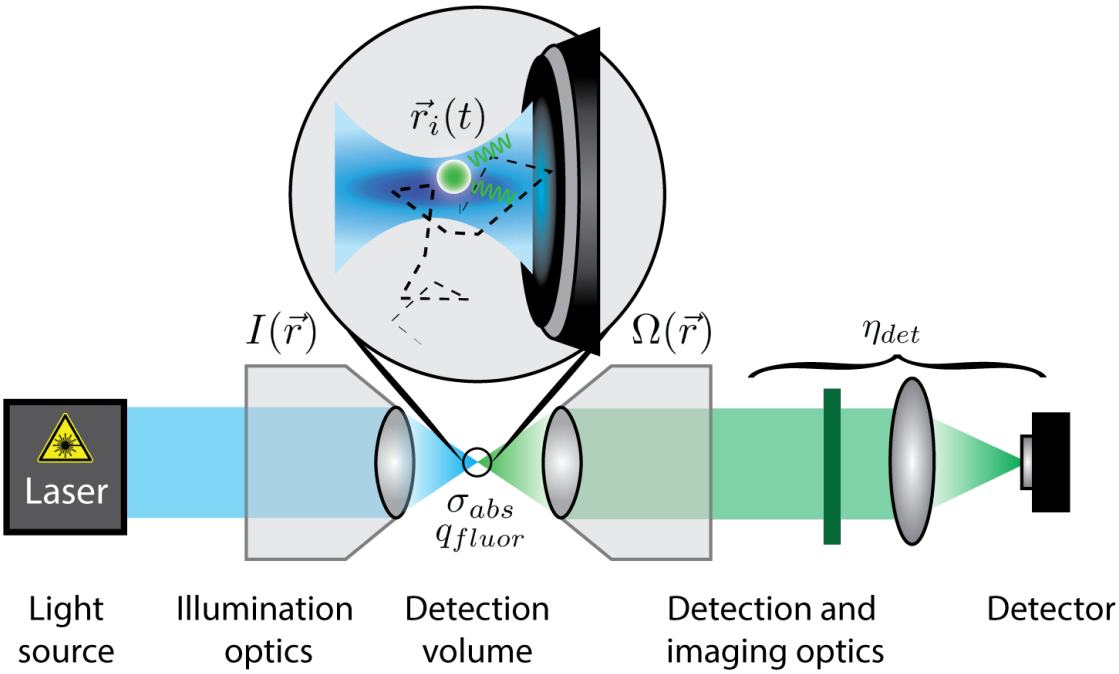

FIGURE 2.1: General excitation and detection setup for FCS experiments. The light source is focused to a specific geometry depending on the illumination optics with an intensity distribution $I(\vec{r})$. The detection is described by two components: the spatially dependent detection efficiency distribution $\Omega(\vec{r})$, and a detection efficiency factor, η_{det}. The molecules i in the sample follow trajectories $\vec{r_i}(t)$, with an absorption cross-section σ_{abs}, and a fluorescence quantum yield q_{fluor}.

be it confocal or SPIM. The detection volume is where molecules of interest are detected by the detection scheme of the microscope, and has a volume denoted V_{sample}. The motion of each molecule in the sample (with N_{sample} molecules in total), is described by its trajectory $\vec{r_i}(t)$. These trajectories are generally inaccessible, however, the statistics related to their motion, such as the mean squared displacement (MSD) is known. The spatial-temporal concentration distribution can be written as:

$$c(\vec{r},t) = \frac{1}{V_{sample}} \cdot \sum_{i=1}^{N_{sample}} \boldsymbol{\delta}[\vec{r} - r_i(\vec{t})], \tag{2.1}$$

where $\boldsymbol{\delta}$ denotes the Dirac delta distribution such that

$$\boldsymbol{\delta}[\vec{r} - \vec{r_i}(t)] = \begin{cases} 0 & \vec{r} \neq \vec{r_i}(t) \\ \infty & \vec{r} = \vec{r_i}(t) \end{cases}$$

which directly implies that the concentration is null when the position $\vec{r}$ of interest does not coincide with the trajectory of any molecule.

The sample is illuminated by a spatially dependent intensity distribution (provided that the laser source is stable, minimizing large temporal intensity fluctuations), denoted $I(\vec{r})$. The fluorescent species in the sample is associated with an absorption cross-section σ_{abs}, and a fluorescence quantum yield q_{fluor}. The amount of fluorescence emitted by a single molecule at position $\vec{r}$ is described by:

$$I(\vec{r}) \cdot \sigma_{abs} \cdot q_{fluor}, \tag{2.3}$$

The detection is described by two components: the spatially dependent detection efficiency distribution, denoted $\Omega(\vec{r})$, and a detection efficiency factor, η_{det}. This factor is dependent on the surfaces the emission light interacts with before reaching the detector. This includes the detection objective, mirrors, filters, and other surfaces in the detection pathway. $\Omega(\vec{r})$ is dependent on the point spread function (PSF) of the microscope setup and the geometry of the detector and the detection pathway. Diffraction limited optics result in a point source in the object plane to be observed as a fuzzy circle in the image plane, called an Airy disc. The PSF is related to the three dimensional shape of this Airy disc: In the case of confocal FCS, the Airy disc is the convolution between the pinhole transmission function and the PSF, and for SPIM-FCS, it is the

convolution between square shape of a camera pixel and the PSF. $I(\vec{r})$ and $\Omega(\vec{r})$ are not observable independently, and are combined into a single function, the Molecular Detection Efficiency function (MDE),

$$MDE(\vec{r}) = I(\vec{r}) \cdot \Omega(\vec{r}). \tag{2.4}$$

The number of fluorescence photons collected from a molecule at position $\vec{r}$ are proportional to MDE($\vec{r}$). The MDE function is thus a mathematical representation of the observation volume.

The PSF, the detection efficiency function, and the MDE of a confocal microscope are classically all described as a triple Gaussian,

$$MDE_{confocal}(\vec{r}) = I_0 \cdot \exp\left(-2 \cdot \frac{x^2+y^2}{\omega_{xy}^2} - 2 \cdot \frac{z^2}{\omega_z^2}\right) \tag{2.5}$$

The shape of the MDE is more complex in the case of a SPIM. Wohland et al. 2010 suggests that a well aligned and properly designed SPIM has a PSF that can be approximated by a Gaussian. However, as previously stated, due to the nature of the camera detector, the square shape of the pixel must be taken into account when determining the MDE for a SPIM:

$$MDE_{SPIM} = I_0 \cdot \left(h_{pixel} \circledast PSF_{SPIM}\right)(\vec{r}) = \iint_{-a/2}^{a/2} PSF_{SPIM}(\vec{r} - \vec{r'})\ dx'dy' \tag{2.6}$$

where a is the width of the pixel in the object plane and $\circledast$ defines a convolution. h_{pixel} represents the camera pixel and defined as follows:

$$h_{pixel} = \boldsymbol{\delta}(z) \cdot \begin{cases} 1 & -a/2 \leq x \leq a/2 \ \ \wedge -a/2 \leq y \leq a/2 \\ 0 & else \end{cases}$$

The convolution integral in Equation 2.6 can be solved analytically to:

$$\mathrm{MDE}_{SPIM}(\vec{r}) = I_0 \cdot \frac{\left[\mathrm{erf}\left(\frac{a-2x}{\sqrt{2}\cdot\omega_{xy}}\right) + \mathrm{erf}\left(\frac{a+2x}{\sqrt{2}\cdot\omega_{xy}}\right)\right] \cdot \left[\mathrm{erf}\left(\frac{a-2y}{\sqrt{2}\cdot\omega_{xy}}\right) + \mathrm{erf}\left(\frac{a+2y}{\sqrt{2}\cdot\omega_{xy}}\right)\right]}{\left[2\cdot\mathrm{erf}\left(\frac{a}{\sqrt{2}\cdot\omega_{xy}}\right)\right]^2} \cdot \exp\left(-2\cdot\frac{z^2}{\omega_z}\right). \tag{2.8}$$

Figure 2.2 shows a cut along the x-axis of the MDE for a SPIM, plotted using Equation 2.8. What is clearly observed is that as the size of a (size of the pixel in the object plane) deviates farther away from the width of the PSF (550 nm in this case), the Gaussian approximation for the MDE no longer holds, instead the MDE assumes a square shape corresponding to that of the pixel. This implies that the physical pixel of the camera should be carefully selected to match the PSF of the microscope to obtain the best possible spatial resolution.

Using the MDE_{SPIM}, we can determine the shape and form of the fluorescence fluctuations from a fluorophore in a SPIM-FCS microscope, using Equation 2.1.

$$F(t) = \iiint MDE_{SPIM}(\vec{r}) \cdot \eta_{det} \cdot \sigma_{abs} \cdot q_{fluor} \cdot c(\vec{r}, t)\, dV \tag{2.9}$$

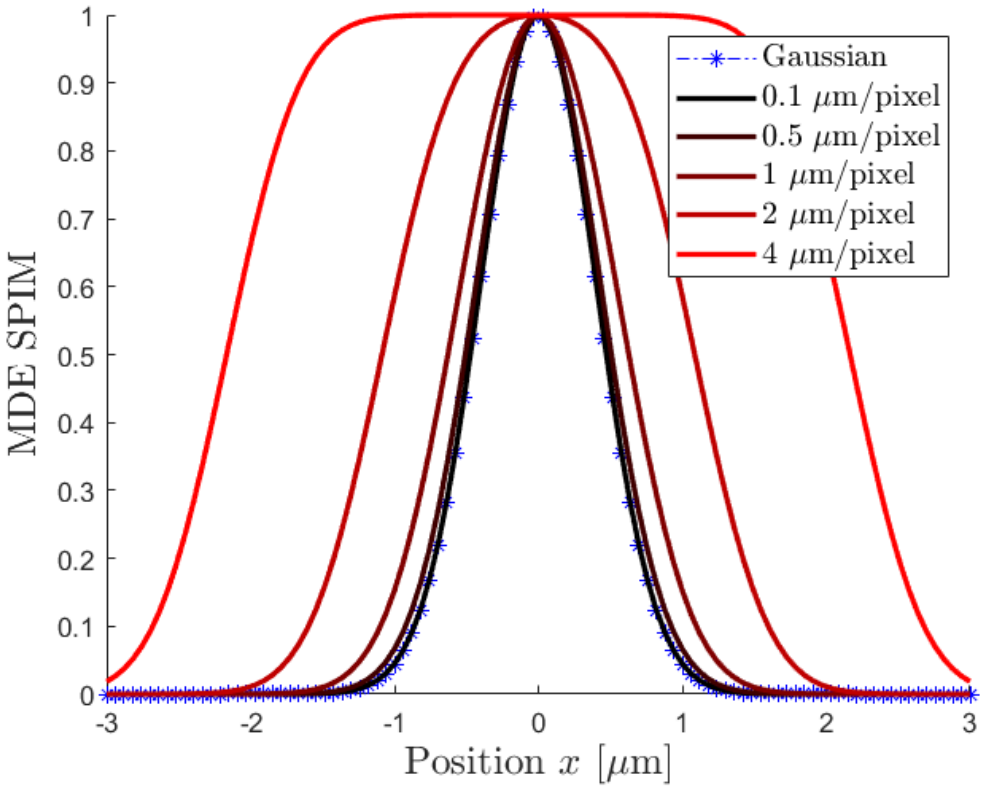

FIGURE 2.2: A cut along the x-axis of the MDE of a SPIM setup plotted using Equation 2.8 and $\omega_{xy} = 550$ nm and $z = 0$.

This can be simplified by using the following definition as the factors η_{det},σ_{abs}, and $\cdot q_{fluor}$ cannot be isolated in an FCS experiment:

$$\eta \equiv \eta_{det} \cdot \sigma_{abs} \cdot q_{fluor}. \tag{2.10}$$

Which leads to:

$$F(t) = \iiint MDE_{SPIM}(\vec{r}) \cdot \eta \cdot c(\vec{r}, t)\, dV. \tag{2.11}$$

The molecule concentration can be rewritten in terms of an average concentration plus a fluctuation term:

$$c(\vec{r},t) = \langle c \rangle + \delta c(\vec{r},t). \tag{2.12}$$

Thus, the fluorescence intensity fluctuations can be written as follows due to the linearity of Equation 2.12,

$$\delta F(t) = \iiint MDE_{SPIM}(\vec{r}) \cdot \eta \cdot \delta c(\vec{r},t)\, dV \tag{2.13}$$

2.2 FCS Autocorrelation Function

Using a similar definition as in Equation 1.13 for the autocorrelation function, we can write the following:

$$G(\tau) = \frac{\langle \delta F(t) \cdot \delta F(t+\tau) \rangle}{\langle F(t) \rangle^2} \tag{2.14}$$

Now, using the results from the previous section, Equations 2.13 and 2.11, we can rewrite the above equation in terms of the MDE,

$$G(\tau) = \frac{\eta \iiint \iiint MDE_{SPIM}(\vec{r}) \cdot MDE_{SPIM}(\vec{r'}) \cdot \langle \delta c(\vec{r},t) \cdot \delta c(\vec{r'},t+\tau) \rangle\, dV\, dV'}{\left(\eta \iiint MDE_{SPIM}(\vec{r}) \cdot \langle c(\vec{r},t) \rangle\, dV\right)^2} \tag{2.15}$$

2.2.1 Zero lag correlation and effective volume

Due to the Poissonian nature of particle (and concentration) statistics in the focal volume, for $\tau = 0$,

$$\langle \delta c(\vec{r},t) \cdot \delta c(\vec{r}',t) \rangle \equiv \langle \delta c^2(\vec{r}',t) \rangle \cdot \boldsymbol{\delta}(\vec{r}-\vec{r}') = \langle c(\vec{r},t) \rangle \cdot \boldsymbol{\delta}(\vec{r}-\vec{r}') \tag{2.16}$$

where the Dirac delta $\boldsymbol{\delta}$ implies that particles are non-interacting and therefore, statistically independent.

Using the condition that the average concentration is constant over the observation volume, the zero lag correlation amplitude can be written as

$$\begin{aligned} G(0) = \frac{\eta^2 \cdot \langle c \rangle \iiint MDE_{SPIM}^2(\vec{r})\, dV}{(\eta \cdot \langle c \rangle \iiint MDE_{SPIM}(\vec{r})\, dV)^2} &= \frac{\eta^2 \cdot \langle c \rangle}{(\eta \cdot \langle c \rangle)^2} \cdot \frac{\iiint MDE_{SPIM}^2(\vec{r})\, dV}{(\iiint MDE_{SPIM}(\vec{r})\, dV)^2} \\ &= \frac{1}{\langle c \rangle} \cdot \frac{\iiint MDE_{SPIM}^2(\vec{r})\, dV}{(\iiint MDE_{SPIM}(\vec{r})\, dV)^2} \end{aligned} \tag{2.17}$$

The definition for the effective volume is introduced for the SPIM system,

$$V_{eff} = \frac{(\iiint MDE_{SPIM}(\vec{r})\, dV)^2}{\iiint MDE_{SPIM}^2(\vec{r})\, dV} = \frac{\langle N \rangle}{\langle c \rangle} \tag{2.18}$$

where $\langle N \rangle$ defines the average particle number in the effective volume. Then,

$$G(0) = \frac{1}{\langle N \rangle} \tag{2.19}$$

Solving the integral equation for the effective volume,

$$V_{eff-SPIM} = \frac{\sqrt{\pi} \cdot a^2 \cdot \omega_z}{\left[\text{erf}\left(\frac{a}{\omega_{xy}}\right) + \frac{\omega_{xy}}{\sqrt{\pi} \cdot a}\left(\text{e}^{-a^2/\omega_{xy}^2} - 1\right)\right]^2} \tag{2.20}$$

2.2.2 Concentration correlation factor

The concentration correlation factor is defined by the following, which describes the particle dynamics in the autocorrelation function:

$$\phi(\vec{r}, \vec{r}', \tau) := \langle \delta c(\vec{r}, t) \cdot \delta c(\vec{r'}, t + \tau) \rangle \tag{2.21}$$

This factor quantitatively describes the correlation at a lag time τ between the concentration fluctuations at two positions $\vec{r}$ and $\vec{r}'$.

The concentration correlation factor is proportional to the van-Hove self correlation function of the particles (Hopkins et al. 2010, Hansen and McDonald 2006), which depends on single particle trajectories $\mathbf{r}(\tau)$, where the probability of finding a particle at position $\mathbf{r}$ at time τ, given that there was a particle at the origin at time $\tau = 0$:

$$P(\mathbf{r}, \tau) = \frac{1}{N}\left\langle \sum_{i=1}^{N_{sample}} \sum_{j=1}^{N_{sample}} \boldsymbol{\delta}[\mathbf{r} + \mathbf{r}_j(0) - \mathbf{r}_i(\tau)] \right\rangle$$

(2.22)

This equation is simplified, where instead of being written in terms of $\vec{r}$ and $\vec{r}'$, it is written as a function of $\mathbf{r}$. So here, $\vec{r}'$ is set to the origin.

The unique forms of $P(\cdot,\cdot)$ are the Green's function of the partial differential equation (PDE) that describes the concentration, $\langle c(\vec{r},t)\rangle$.

The concentration correlation factor is then given by,

$$\phi(\vec{r},\vec{r}',\tau) = \langle c\rangle \cdot P(\vec{r},\vec{r}',\tau) \tag{2.23}$$

With these formulations, Equation 2.15 can be written as,

$$G(\tau) = \frac{\eta\langle c\rangle \iiint \iiint MDE_{SPIM}(\vec{r}) \cdot MDE_{SPIM}(\vec{r'}) \cdot \phi(\vec{r},\vec{r}',\tau)\, dV\, dV'}{(\eta\langle c\rangle)^2 \cdot \left(\iiint MDE_{SPIM}(\vec{r})\, dV\right)^2} \tag{2.24}$$

$$g(\tau) = \frac{\eta^2 \cdot G(\tau)}{(\eta\langle c\rangle)^2} \tag{2.25}$$

Where $g(\tau)$ is the non-normalized correlation function of the fluctuations $\delta F(t)$ of a single species in a single channel wavelength,

$$\begin{aligned} G(\tau) &= \frac{\langle \delta F(t) \cdot \delta F(t+\tau)\rangle}{\eta^2 \cdot (\iiint MDE_{SPIM}(\vec{r})\, dV)^2} \\ &= \langle c\rangle \cdot \frac{\iiint \iiint MDE_{SPIM}(\vec{r}) \cdot MDE_{SPIM}(\vec{r'}) \cdot \phi(\vec{r},\vec{r}',\tau)\, dV\, dV'}{(\iiint MDE_{SPIM}(\vec{r})\, dV)^2} \end{aligned} \tag{2.26}$$

2.3 Normal Diffusion

This section will provide explicit formulae for the concentration correlation factor and the autocorrelation function for a MDE_{SPIM} for fluorescent particles undergoing normal Brownian motion as described in Section 1.1.1.

In normal diffusion, the particle concentration is determined by the diffusion equation,

$$\frac{\partial(\langle c\rangle + \delta c(\vec{r},t))}{\partial t} = D\cdot\vec{\nabla}^2(\langle c\rangle + \delta c(\vec{r},t)) \tag{2.27}$$

$$\frac{\partial \delta c(\vec{r},t)}{\partial t} = D\cdot\vec{\nabla}^2\delta c(\vec{r},t) \tag{2.28}$$

This has the Green's function,

$$P(\vec{r},\vec{r}',\tau) = \frac{1}{(4\pi D\tau)^{3/2}}\cdot\exp\left(\frac{(\vec{r}'-\vec{r})^2}{4D\tau}\right) \tag{2.29}$$

Using this, the ACF for normal diffusion can be calculated for a SPIM-FCS system. The MDE_{SPIM} and Equation 2.29 can be separated into three factors that depend on the directions x, y or z, so the normalized ACF $G(\tau)$ can also be separated:

$$G(\tau) = \frac{1}{\langle c\rangle}\cdot g_x(\tau)\cdot g_y(\tau)\cdot g_z(\tau) \tag{2.30}$$

with each factor defined by (and indexed by χ for each direction),

$$g_\chi(\tau) = \frac{\iint MDE_\chi(\xi)\cdot MDE_\chi(\xi')\cdot\phi_\chi(\xi,\xi',\tau)\,d\xi\,d\xi'}{(\int MDE_\chi(\xi)\,d\xi)^2}. \tag{2.31}$$

For a SPIM-FCS, along the z-direction, the MDE is Gaussian, so $g_z(\tau)$ is given by,

$$g_z(\tau) = \frac{1}{\sqrt{\pi}\cdot\omega_z}\cdot\left(1+\frac{4D\tau}{\omega_z^2}\right)^{-1/2}. \tag{2.32}$$

For the x and y-directions, which are equivalent,

$$g_x(\tau) = g_y(\tau) = \frac{1}{a}\cdot\left\{\text{erf}\left(\frac{a}{\sqrt{4D\tau+\omega_{xy^2}}}\right)+\frac{\sqrt{4D\tau+\omega_{xy}^2}}{a\cdot\sqrt{\pi}}\left[\exp\left(-\frac{a^2}{4D\tau+\omega_{xy}^2}\right)-1\right]\right\}. \tag{2.33}$$

Thus, the 3-dimensional normalized ACF is,

$$G(\tau) = \frac{1}{\langle c\rangle\cdot\sqrt{\pi}\cdot\omega_z\cdot a^2}\left\{\text{erf}\left(\frac{a}{\sqrt{4D\tau+\omega_{xy^2}}}\right)+\frac{\sqrt{4D\tau+\omega_{xy}^2}}{a\cdot\sqrt{\pi}}\left[\exp\left(-\frac{a^2}{4D\tau+\omega_{xy}^2}\right)-1\right]^2\right\} \cdot\left(1+\frac{4D\tau}{\omega_z^2}\right)^{-1/2} \tag{2.34}$$

Using the definition for the concentration ($\langle c\rangle = \langle N\rangle/V_{eff}$), we can rewrite this in terms of the absolute number of particles in conjunction with the definition of the effective volume for a SPIM through Equation 2.20.

Determining the diffusion time, τ_D, of the molecules in the excitation volume is non-trivial due to the complex shape of the MDE. The following definition is used in Wohland et al. 2010:

$$\tau_D = \frac{A_{eff}}{4D} \tag{2.35}$$

where A_{eff} is the effective lateral focal area, defined by:

$$\begin{aligned} A_{eff} &= \frac{\left(\iint MDE_{SPIM}(x,y,0)\,dx\,dy\right)^2}{\iint MDE^2_{SPIM}(x,y,0)\,dx\,dy} \\ &= \frac{a^2}{\left[\mathrm{erf}\left(\frac{a}{\omega_{xy}}\right) + \frac{\omega_{xy}}{\sqrt{\pi}\cdot a}\left(\mathrm{e}^{-a^2/\omega_{xy}^2} - 1\right)\right]^2} \end{aligned} \tag{2.36}$$

This definition does not satisfy the $G(\tau_D) = G(0)/2$ but is useful, since a closed form definition of τ_D that satisfies the half amplitude condition is not possible.

Below are plots of Equation 2.34 with varying parameters.

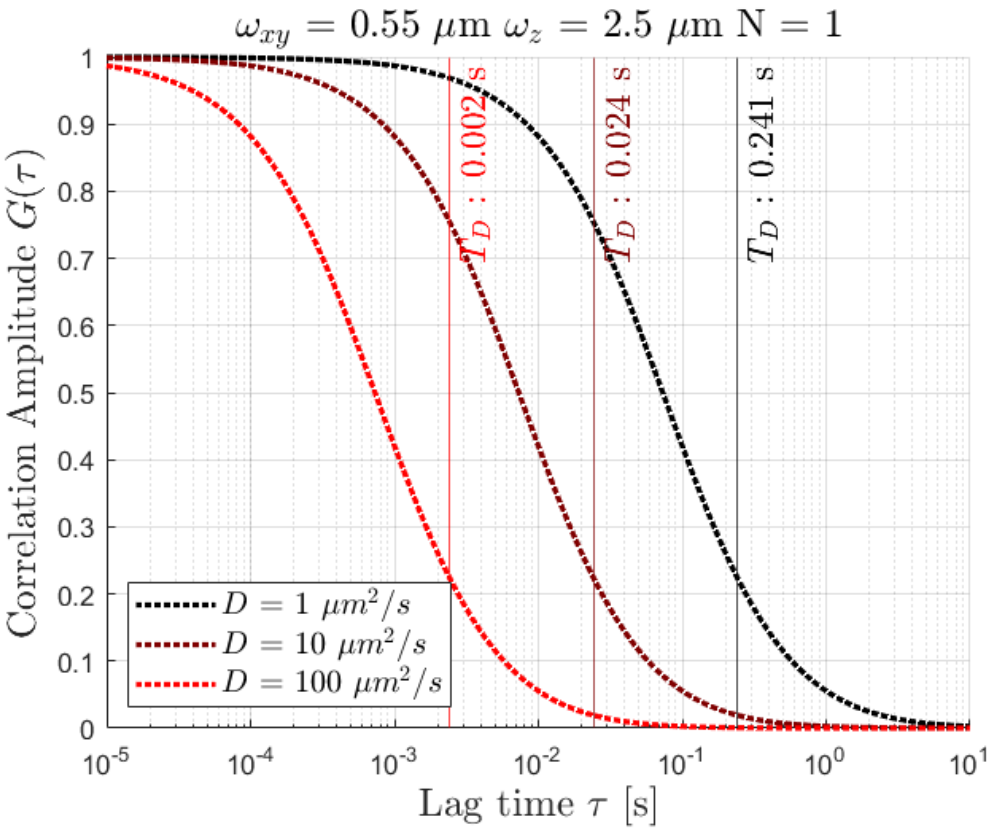

FIGURE 2.3: Varying the diffusion coefficient while keeping $\omega_{xy} = 550$nm, $\omega_z = 2500nm$, and $\langle N \rangle = 1$. Vertical lines show the dwell time.

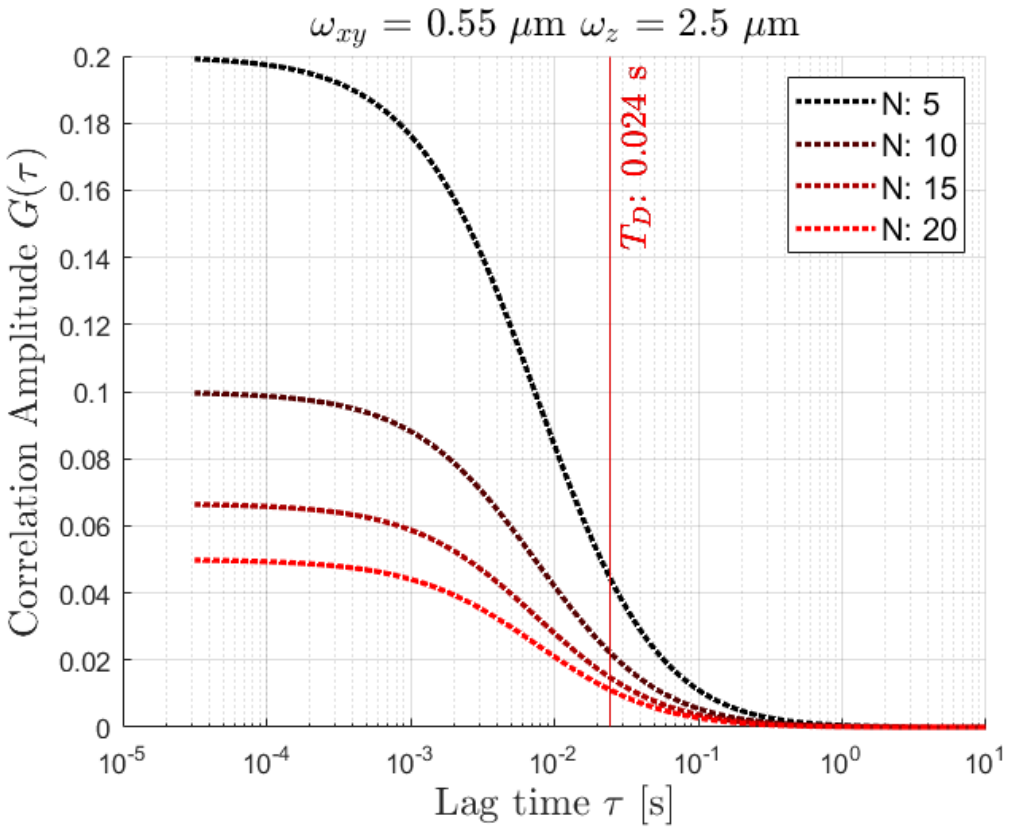

FIGURE 2.4: Varying the average number of particles while keeping $\omega_{xy} =$ 550nm, $\omega_z = 2500nm$, and $D = 10\ \mu m^2/s$. Vertical lines show the dwell time.

Comparing the normalized ACFs for a confocal FCS (Equation 1.15) and a SPIM-FCS (Equation 2.34), they both yield the same information, the diffusion coefficients D, and the average concentration, $\langle c \rangle$, provided that both instruments are calibrated such that we have accurate estimates for the physical parameters (ω_{xy}, ω_z, and a for SPIM-FCS) that defines the 3 dimensional PSF.

Part II

SPIM-FCS: Development and Instrumentation

Chapter 3

SPIM-FCS Hardware

Over the course of this Masters project, a single plane illumination microscope (SPIM) was designed and built for the purpose of performing image fluorescence correlation spectroscopy (imFCS). In the previous chapter, I explicitly derived the formulae that would yield dynamical parameters of interest, the diffusion coefficient and concentration, for a SPIM-FCS. To extract these values, ACF curves are fitted with appropriate models, given that the optics are carefully aligned and the microscope is calibrated such that we have accurate estimates of the PSF parameters, ω_{xy}, ω_z, and a. This chapter will describe the instrument design and hardware that was meticulously planned such that ω_{xy}, ω_z, and a could be estimated with accuracy and repeatability. The chapter is split into three sections: The illumination optics is described in Section 3.2, the sample chamber in Section 3.3, and the detection scheme in Section 3.4, with a focus on camera readout electronics. Section 3.5 is dedicated to data analysis. Lastly, in Section 3.6, I will show the results of experiments done to characterize the physical properties of the light sheet produced in our SPIM-FCS instrument.

3.1 Overview

This section will provide a large scale overview of our SPIM-FCS instrument shown in Figure 3.1. I have also rendered the optical setup in AUTOCAD 2020, focusing on optical components after the beam expander, and this is shown in Figure 3.2. The light sheet is generated by a super-continuum white laser source (and according filters for precise excitation) and shaped by the combination of a cylindrical lens and an air objective. The fluorescence is detected by a high numerical aperature (NA) water dipping objective (and according filters for precise emission) and captured by a sCMOS camera. The sample is suspended in a liquid filled chamber (deionized water or 1X PBS buffer), which rests on XZ translation stages. The sample itself is attached to a XYZ-θ stage. The SPIM-FCS setup rests on a floating optical table to actively dampen vibrations.

3.2 Illumination arm

The illumination arm was designed to allow for maximum control over the position of the light sheet by steering the beam into the back aperture of the objective with mirrors. Furthermore, the open concept of seeing the beam expander at all times allows for direct visualization of the beam path, so that it may be corrected should the beam be optically non ideal. An example of this would be if the beam was not passing through the center of the lenses. A Fianium super-continuum laser is used as the white light laser source (SC-450-PP-HE,Fianium INC, USA). The intensity of the beam is electronically adjustable allowing for consistent measurements. Large parts of the power spectrum of the laser source exist in the infrared range, and thus a filter specifically designed to block this region is placed immediately after the laser.

The laser beam is then filtered with a 480 $\pm$ 15 nm band pass filter to select the range of excitation wavelengths. The filtering of both the visible and IR region is done in an enclosed box denoted by the grey box in Figure 3.1. Since this is a supercontinuum

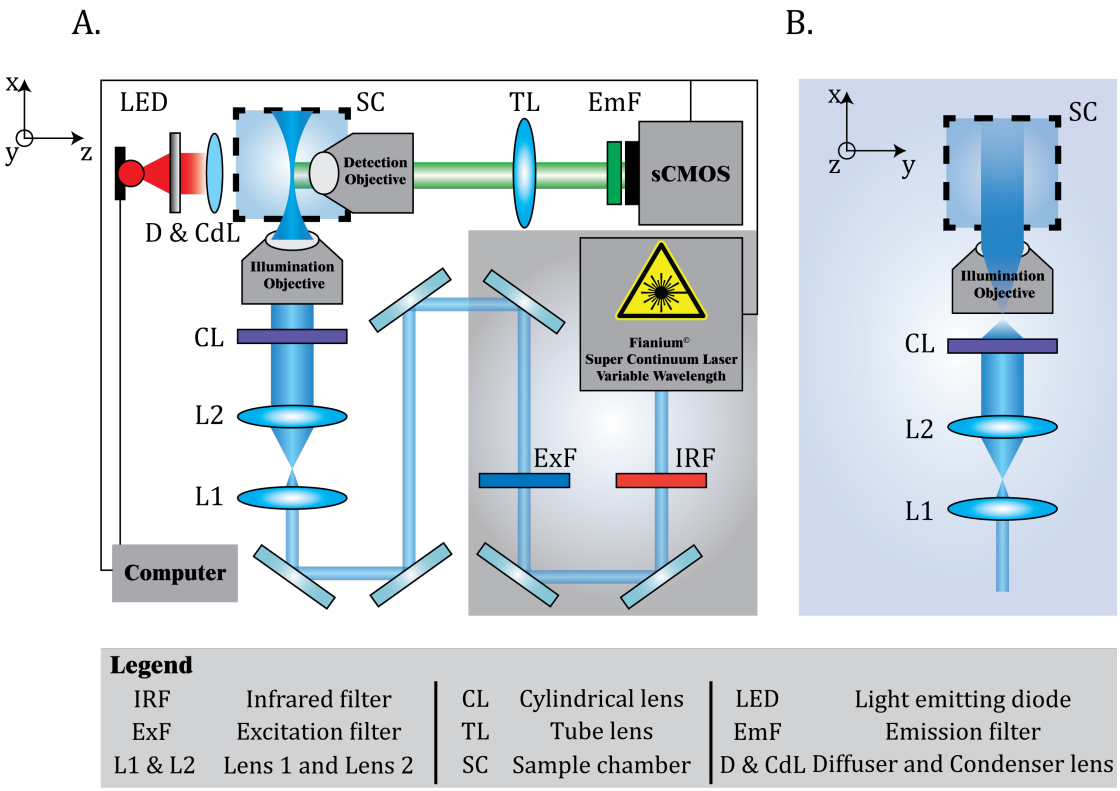

FIGURE 3.1: **A.** Entire optical setup (top view). The legend contains the abbreviations used for optical components. Black lines represent electronic wire connections from various components to the computer. **B.** Side view of the illumination beam path. Objects and distances are not to scale.

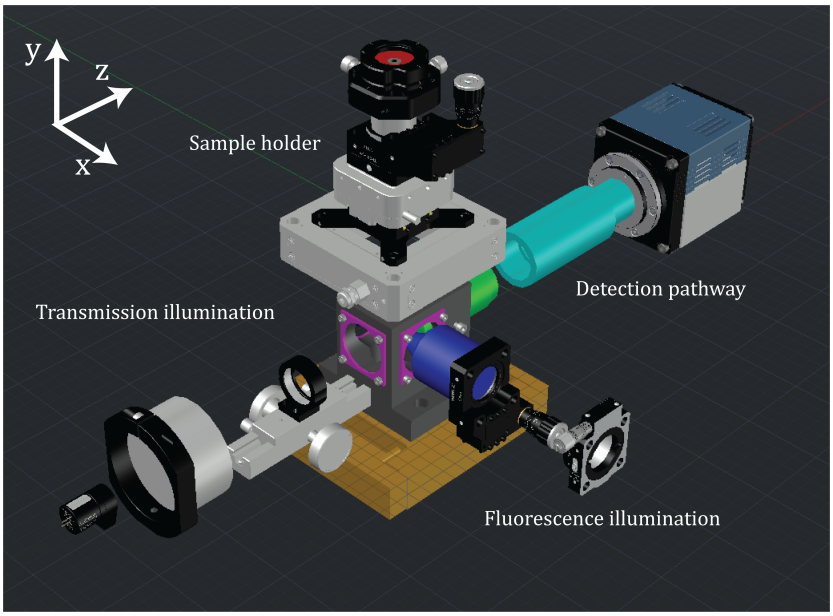

FIGURE 3.2: AUTOCAD rendering of the optical setup, after the beam expansion.

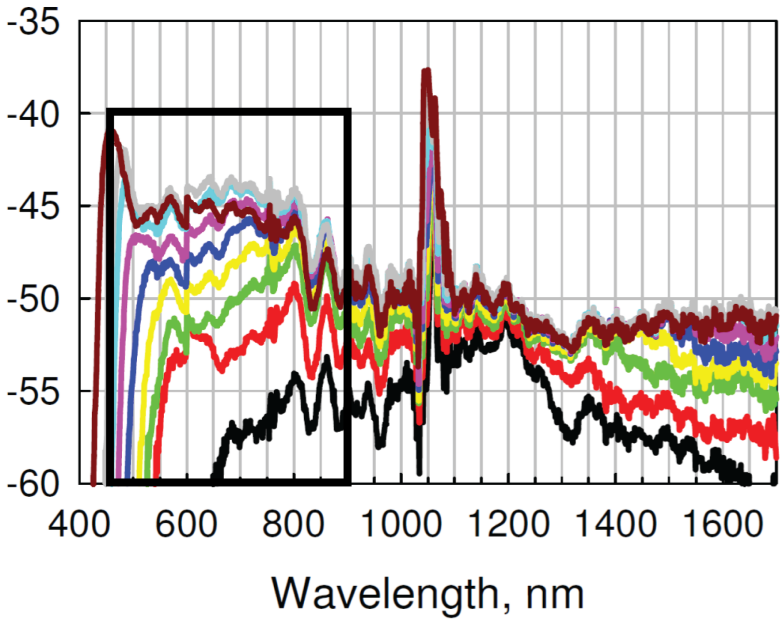

FIGURE 3.3: Spectral power density of the super-continuum laser source used for fluorescence excitation. Note the large peak in the 1000 to 1100 nm range which must be blocked out using an infrared filter. The black curve indicates lower power, ranging to higher power with the brown curve. The black box indicates the wavelengths accessible after IR blocking.

laser, instead of a single wavelength, the entire bandwidth of the excitation filter is used to fluorescently excite the samples.

The beam is then brought to an appropriate height in y through a periscope. This is then reflected off of two mirrors used for adjusting the position and direction of the beam. Then, it is expanded using two lenses, $L1$ and $L2$ with focal lengths $f_{L1} = 50$ mm and $f_{L2} = 100$ mm, and focused using a cylindrical lens (CL) with focal length $f_{CL} = 150$ mm and the illumination objective, OLYMPUS 10X, 0.25 NA air objective with a large working distance of 21 mm. The distance of the last two lenses is adjusted, so that the focus of the cylindrical lens coincides with the back-focal point of the illumination objective. The cylindrical lens is mounted on a precise rotation mount (CRM1P/M, Thorlabs) to obtain the correct orientation of the light sheet. The illumination objective is mounted on a translation mount with 1 μm resolution and 2 mm travel. This allows for accurate positioning of the focus of the light sheet, such that it coincides with the imaging plane of the detection objective.

The geometry of the light sheet radius is described by the following equation (Pedrotti and Pedrotti 1993),

$$\omega(x) = \omega_0 \left(1 + \left(\frac{\lambda x}{\pi \omega_0^2}\right)^2\right)^{1/2} \tag{3.1}$$

where $\omega(x)$ is beam radius at which the intensity drops to $1/e^2$ of the axial value, ω_0 is the $1/e^2$ light sheet radius at the focus, and λ is the illumination wavelength, where e is Euler's number. This equation can be derived by treating the laser beam as a Gaussian beam using the angular spectrum representation method under the paraxial beam approximation (Pedrotti and Pedrotti 1993). The shape of the beam is illustrated in Figure 3.4. Using the specifications of the illumination objective, an approximation

of the $1/e^2$ beam half-width, ω_0 (Wolfgang Krieger 2014),

$$\omega_0 \approx 0.82\frac{\lambda}{NA} \tag{3.2}$$

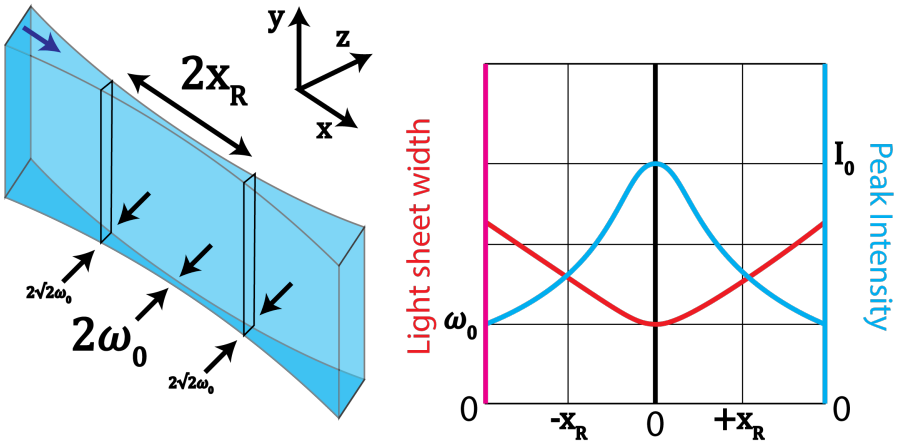

FIGURE 3.4: Rendering of the geometry of a light sheet. The graph on the left describes the intensity (in blue) and thickness (in red) as a function of displacement from the focus of the beam. Image provided by Jan Krieger, 2013.

The Rayleigh range x_R defined as the distance from the focus to the point where the radius has increased by a factor of $\sqrt{2}$. The field of view (FOV) is defined as twice the Rayleigh range ($2x_R$) and can be approximated as (Wolfgang Krieger 2014):

$$FOV = 2 \cdot x_R \approx 2 \cdot 2.8 \cdot \frac{\lambda}{NA^2} \tag{3.3}$$

For my system, $\lambda = 488$ nm and $NA = 0.25$,

$$\omega_0 \approx 1.6\,\mu m \qquad\qquad FOV \approx 43.7\,\mu m \tag{3.4}$$

The height of the light sheet when viewed in the xz-plane can be determined through,

$$h_{LS} = w_{laser} \cdot \frac{f_{L2}}{f_{L1}} \cdot \frac{f_{IllObj}}{f_{CL}} = 2\,mm \cdot \frac{100}{50} \cdot \frac{21}{150} \approx 0.56\,mm \tag{3.5}$$

where w_{laser} is the diameter of the laser beam out of the laser box, and f_{IllObj} is the focusing length of the illumination objective.

Non-fluorescent illumination and imaging of the sample is done through a white light LED source, a diffuser, and s condenser lens. This is shown in Figure 3.5 as the transmission illumination along the z-axis. In the same figure, you see along the x-axis the cylindrical lens on a rotation mount, the illumination objective on the x-translation mount, and the sample chamber.

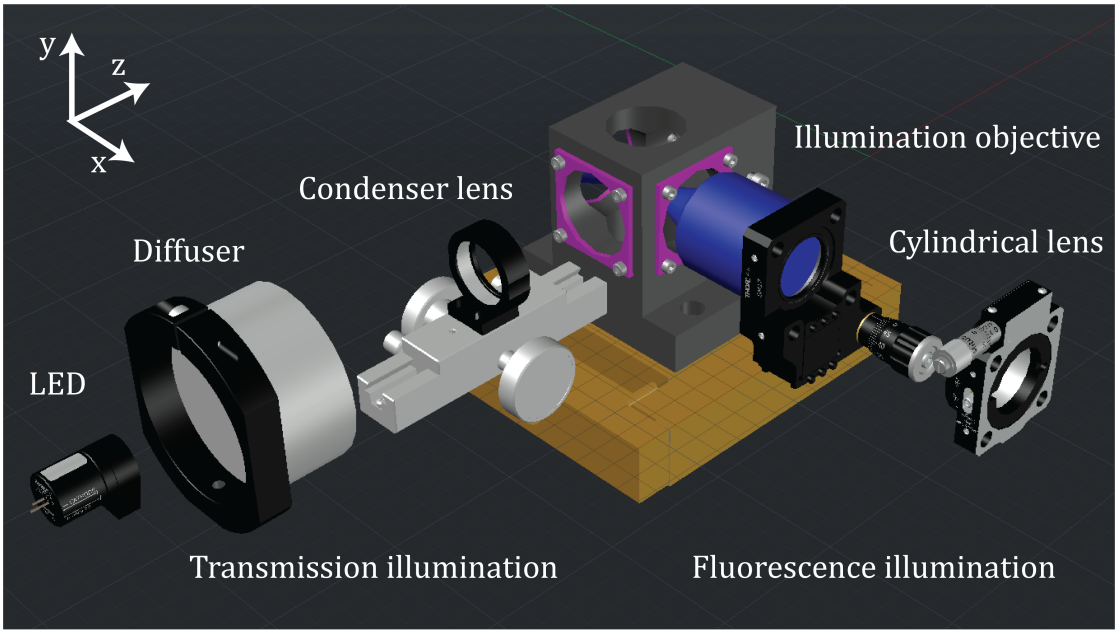

FIGURE 3.5: AUTOCAD rendering of the illumination arms displaying both fluorescence and transmission illumination.

3.3 Sample chamber and mounting

The sample chamber used in this setup is shown in Figure 3.6 as the AUTOCAD rendering and the finished product. The chamber was designed by me and inspired by the work of Dr.Jan Krieger, and manufactured by the Engineering Machine Shop at McMaster University. It is made in stainless steel to prevent corrosion and rusting due to the use of saline buffers. Stainless steel also provides low thermal conductivity which maintains a constant temperature of the solution inside the chamber. The sample chamber has 5 holes. The top hole is the entrance for the suspended sample. There are three holes which are windows covered by removable 0.17 mm thickness glass cover slips that allow for the light sheet to enter on one side and for the light for transmission illumination to enter on another. The last hole covered by glass is an aid for sample and light sheet visualization and sample positioning. The wall of the sample chamber where the detection objective is inserted was made much thicker to provide stability for the objective itself, and as a way to prevent leaks from the chamber. This objective is held in place by hand tightened plastic screws (so as not to damage the casing of the detection objective). This hole for the detection objective is seen in the picture of the finished chamber (bottom half of Figure 3.6). The detection objective used is a 60X 1.0 NA water dipping objective with a working distace of 2 mm (LUMPLFLN60XW, Olympus).

The sample mounting was designed by me and inspired by the mounting used by OpenSPIM, specifically for this open SPIM-FCS system. OpenSPIM is an open access platform by Jan Huisken and Pavel Tomancak. It is illustrated by an AUTOCAD rendering in Figure 3.7. I will describe this sample holder from the bottom to the top. First is a xz piezo nanopositioner with 0.1 nm resolution and 100x100 μm travel range (P-733.2CL, Physik Instrumente), which allows for precise movement of the sample though analog voltage inputs. This is held above the sample chamber by a metal plate and optical posts. The high translational resolution allows for characterization of the

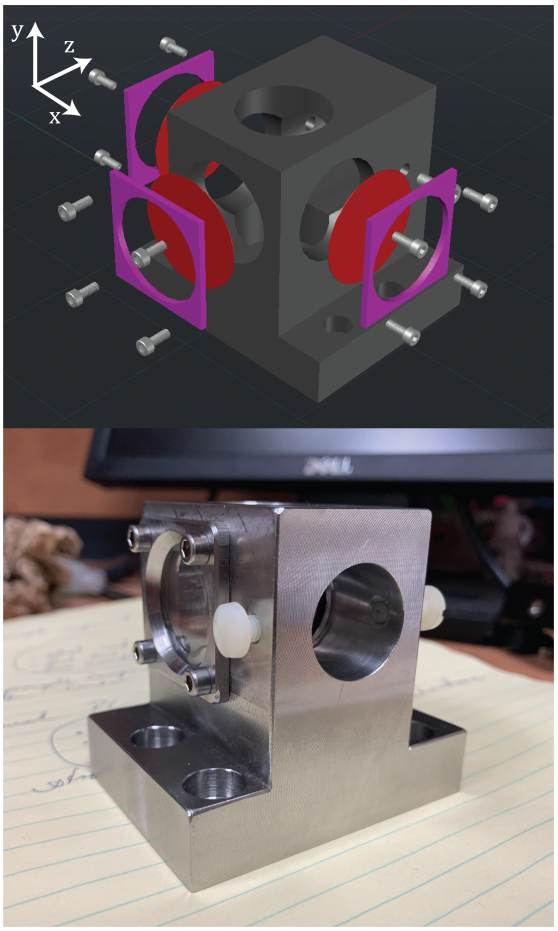

Figure 3.6: **Top** AUTOCAD rendering of the sample chamber using an exploded view. **Bottom** Stainless steel sample chamber used in our SPIM-FCS setup.

MDE which is described in Section 3.6. An adapter (LCP4S, Thorlabs) is used and modified (additional holes drilled) to screw on a high precision rotation stage (PR01, Thorlabs).The stage can be smoothly and continuously rotated through a full 360°, with 1° graduation marks on the side of the stage. There is also a micrometer which provides ±5° degrees of fine adjustment, measured with 5 arcmin resolution by a vernier scale. Connected to the rotation mount is a z translation with 1 μm resolution and with 2 mm travel (SM1Z, Thorlabs) which is coupled to a coarse xy translating mount with a ±1 mm travel range and magnetic quick release (CXY1Q, Thorlabs). The rotation mount has taps for a 30 mm cage system allowing to connect the y and xz translation mounts to it which gives a coarse y adjustment by hand, and a fine y adjustment through the y translation mount.

The sample itself is held through the use of a stereotaxic cannula holder which is generally intended for optogenetics (XCF and XC7, Thorlabs). However, I take advantage of its 2.5 mm opening which can tightly hold capillaries and other cylindrical objects up to 4 mm through its vice mechanism. This is shown in Figure 3.8 as the silver components. A custom sample adapter designed by me was made (shown in red in Figure 3.8) which allows the cannula holder to be held in the magnetic quick release mount as shown in Figure 3.7. This allows me to place and remove the sample quickly and efficiently without disturbing the rest of the sample holding setup. In this way, 3D samples can be held in the capillary though gelling mediums, and aqueous samples can be held in transparent bags using a clamp attached to a metal rod which can be fit inside the cannula holder. Sample preparation is described in greater detail in Part III.

Lastly, the sample chamber is on two coupled linear stages (XR25C, Thorlabs) which allow for the sample chamber and the embedded detection objective to be moved in the xz plane with a travel range of 25 mm and a 500 μm displacement with every full revolution of the displacement knob. The attached micrometer (150-801ME-H, Thorlabs) yields a

resolution of 10 μm per division. This allows to bring samples into focus.

3.4 Detection arm

The detection arm of the SPIM-FCS setup implements a widefield detection scheme. It begins with the water dipping objective (Olympus 60X, 1.0 NA) embedded into the sample chamber. The light collected from the objective is focused onto a camera chip through the tube lens. The tube lens used is a super wide tube lens (SWTLU-C, Olympus) which offers a larger field of view (26.5 mm) compared to a classical tube lens (22 mm) when used with UIS2 objectives from Olympus. The light is then filtered by an emission filter (520 nm high pass filter), so that only the selected wavelengths will be detected by the camera chip. The tube lens and filter are housed in an aluminum couple cylinder part attached directly to a C-mount which screws into the opening port of the camera. This is shown in Figure 3.9. This was designed by me and manufactured by the McMaster Engineering Machine Shop. The rendering is shown in Figure 3.4.

The camera used for the detection is an Hamamatsu ORCA Flash 4 V3 sCMOS camera. The following subsection will be used to describe the camera in greater detail.

3.4.1 Camera readout

As stated earlier, the camera used for detection is the Hamamatsu ORCA Flash 4 V3 sCMOS. This is a 2048 by 2048 camera sensor, with the physical size of each pixel being 6.5 μm. In the object plane, with a 60X detection objective, each pixel is 108 by 108 nm in size. Singh et al. 2013 performed a study of comparing multiple 2D array detectors for the purpose of SPIM-FCS. This camera was chosen specifically for its small pixel size (which can later be binned), fast frame rates, and high sensitivity that can be improved upon by enhanced cooling methods.

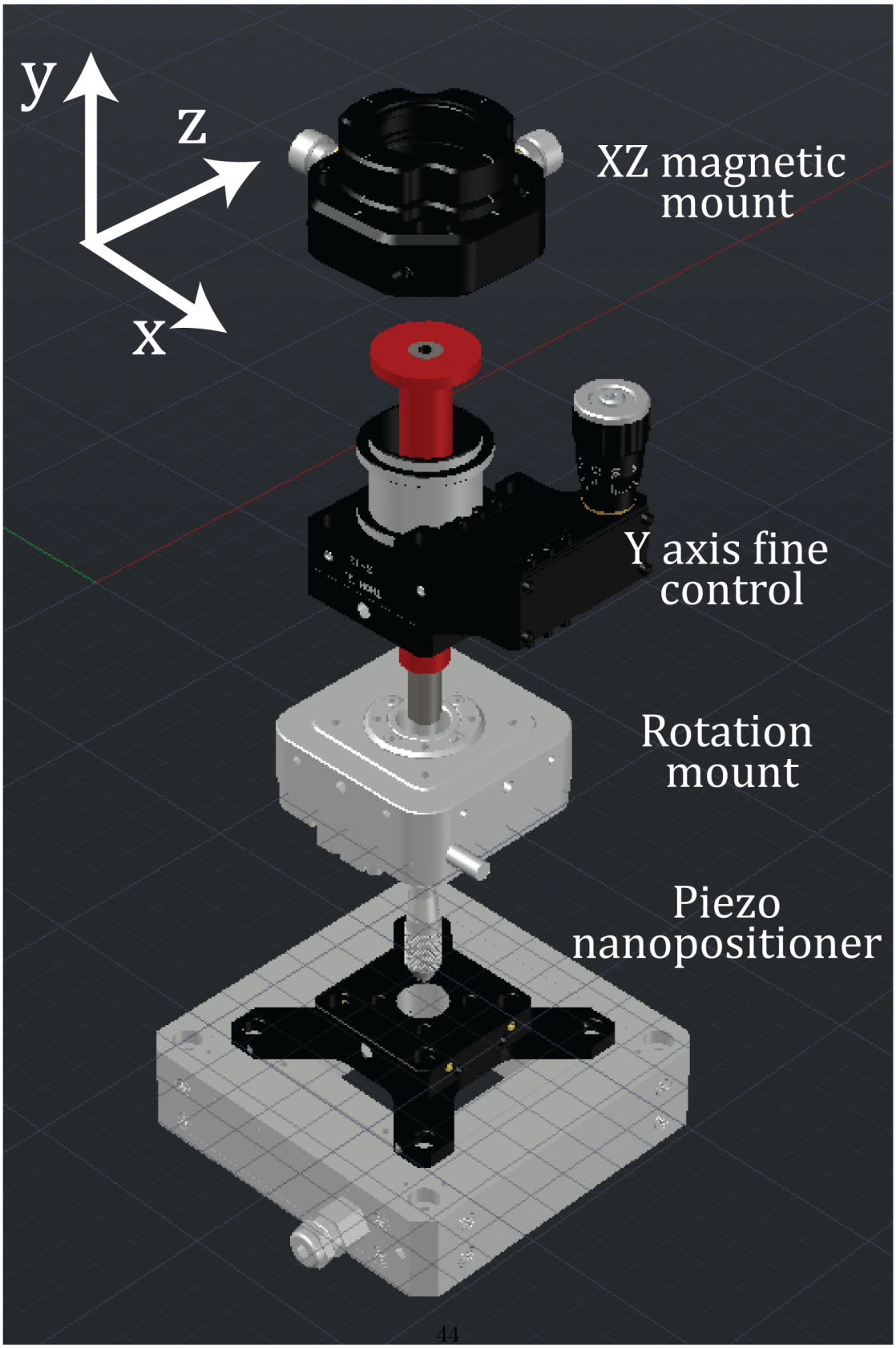

Figure 3.7: AUTOCAD rendering of the sample holder using an exploded view to show all aspects.

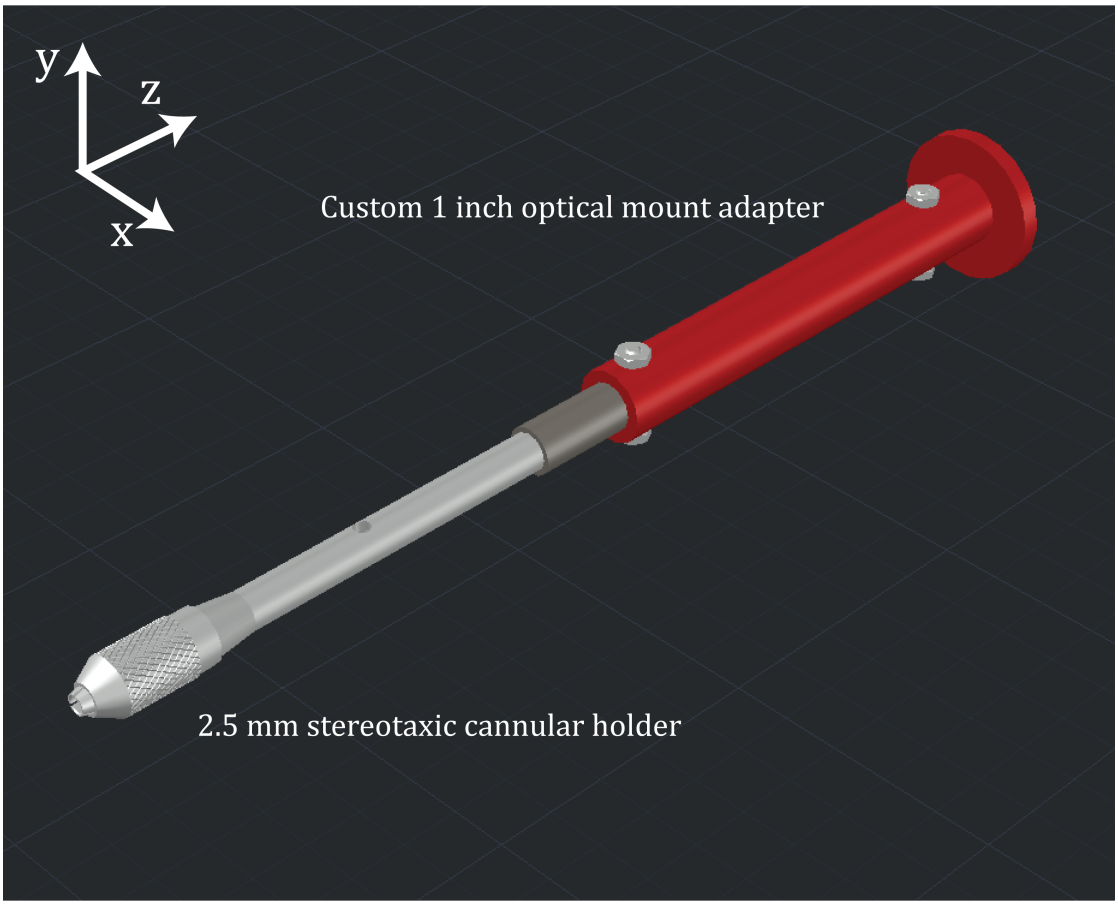

Figure 3.8: AUTOCAD rendering of the sample holder adapter to optical mounts made for one inch optics.

Figure 3.9: Tube lens and emission filter holder. **A.** The three components of the tube lens holder and emission filter holder. The topmost piece is the C-mount which attaches to the camera, the middle piece allows for an adjustable length to accurately place the tube lens away from the camera chip which is held in the last piece. **B.** and **C.** A specially made filter holder slides into the tube so that it is placed right where the end of the C-mount is inside the tube. **D.** Assembled holder.

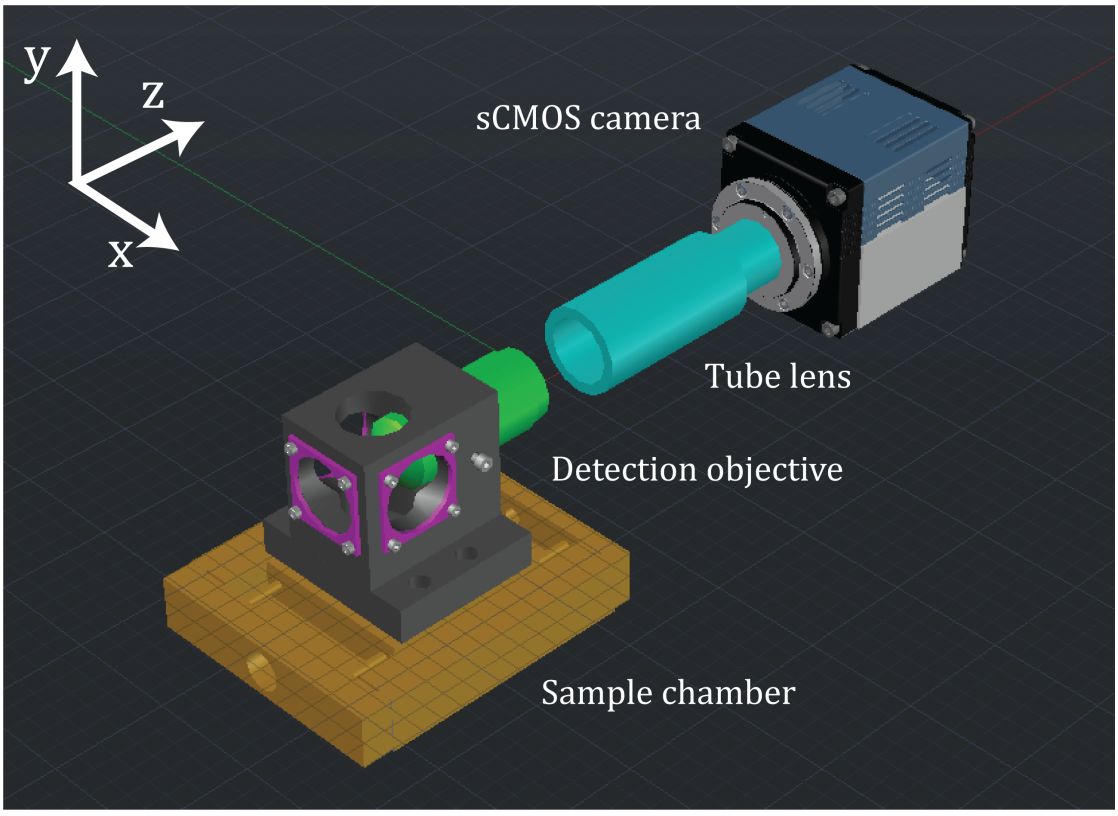

FIGURE 3.10: AUTOCAD rendering of the detection arm.

Each pixel in a CMOS sensor is comprised of a photodiode and an amplifier which converts the charge (a product of the light detected by the photodiode) into a voltage. The voltage of each pixel is output by flipping the switch one by one, as shown in Figure 3.11. Specifcally for this camera, low noise and high speed readout is achieved through on-chip correlated double sampling (CDS). This is done by reading the top and bottom halves of the camera chip independently, and each horizontal line on the camera chip is read by both CDS and A/D (analogue/digital) on the top and bottom in parallel and simultaneously (Hamamatsu Photonics K.K. 2018).

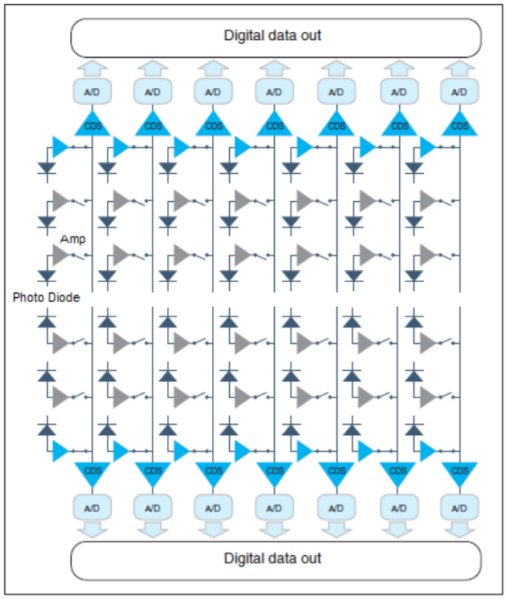

FIGURE 3.11: Structure of a CMOS sensor. Note the switches adjacent to the amplifier denoted by the right facing grey triangle. These switches are turned on one by one to convert the charge into a voltage. Figure provided by (Hamamatsu Photonics K.K. 2018.)

The readout method of this sCMOS sensor is a rolling shutter, where the exposure and readout are done line by line horizontally. That means that there is a small time delay between the readout of adjacent lines. This delay is 9.7 μs for this camera. For the purpose of imaging FCS, if the characteristic time (approximated by Equation 2.35) is significantly larger than the readout time, then there is no significant influence of the

readout delay on the ACF. This would not, however, hold for very fast objects, or for signals obtained by binning together many pixels.

In free running mode, the frame rate in frames per second (FPS) can be calculated using the following formula,

$$FPS_{free\ \ run\ \ mode} = \frac{1}{V_n/2 \cdot \delta} \tag{3.6}$$

where V_n is the total number of horizontal lines from the center of the image sensor, and δ is the time delay between line readout which equals 9.74436 μs. For example, if a ROI of 100 100 pixels was chosen at the center of the camera chip, then,

$$FPS_{free\ \ run\ \ mode} = \frac{1}{100/2 \cdot 9.7\ \ [\mu s]} = 2052\ \ FPS \tag{3.7}$$

Thus, the fastest frame rate is 25655 FPS for a FOV of 8 lines along the center of the camera chip, which allows for a temporal resolution of 38.9 μs. Since the camera chip is readout line by line, the entire horizontal line is accessible during the readout which allows for large scale multiplexing of FCS at high FPS through imaging.

Figure 3.12 shows the quantum efficiency (QE), a measure of the conversion of incident photons on the light sensitive area of the sensor and the charge carriers collected at the terminals of the sensor. The ORCA Flash 4 V3 has a QE peak of 82 % at a wavelength of 560 nm. This is beneficial as the samples used in this thesis have an emission spectrum peaked around 560 nm.

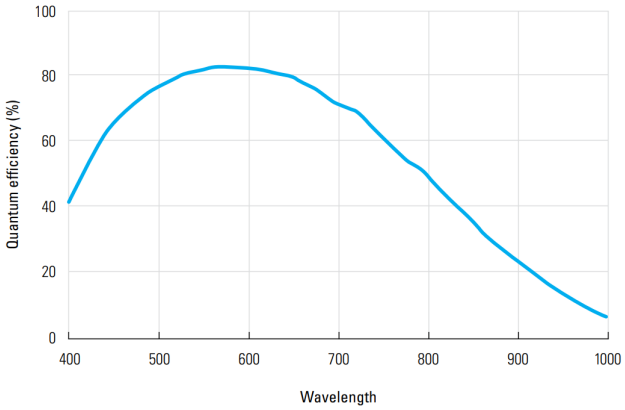

FIGURE 3.12: Quantum efficiency as a function of wavelength for the ORCA Flash 4 V3 sensor. The camera has a peak QE of 82 % at 560 nm. Figure provided by (Hamamatsu Photonics K.K. 2018.)

3.5 Data processing through QuickFit 3.0

The data analysis was performed by using a program developed by Dr. Jan Krieger called QUICKFIT 3.0 (accesible through https://github.com/jkriege2/QuickFit3). It has many capabilities for analyzing various data from a variety of microscopes. This includes FCS curves from a confocal microscope, to imaging FCS image stacks from SPIM or TIRFM (total internal reflection fluorescence microscopy). It also contains routines that aid in performing calibration processes such as determining the light sheet thickness, as well as, the PSF of a given optical setup. I used this program extensively for image correlation, function fitting, and calibration purposes.

It is important to note the data limitations of QUICKFIT 3.0. It will not correlate image stacks larger than 2 GB in size. The size of the image stack is entirely dependent on the number of pixels read, and how many frames (ie. how long the experiment is run). Typically, a 16 bit, 8×500 ROI (an exposure time of 38 μs), with 250, 000 frames yields a file size of just under 2 GB.

3.6 Light sheet characterization

The physical geometry of the light sheet produced by the instrument was determined experimentally in two ways: 1) by performing a mirror scan and 2) by imaging fluorescent beads. The mirror scan yields the $1/e$ half-width of the light sheet, while the bead imaging help determine the PSF of the instrument including the $1/e^2$ height of the PSF along the detection optical axis (z-axis in the AUTOCAD renderings) which correspond to the $1/e^2$ half width of the light sheet by multiplying the $1/e$ half-width of the light sheet by a factor of $\sqrt{2}$. This section will provide detailed explanation on both methods, and the experimental information they provide.

3.6.1 Measuring light sheet thickness with a mirror scan

If a mirror is placed at a 45° angle from the xz plane, where the illumination path denotes the 0°, and the detection path denotes the 90°, image of the cross section of the light sheet can be projected onto the camera and the thickness of the light sheet can be directly measured from this image. By scanning the mirror along the x axis (along the illumination path), one can check how this thickness varies along this path. Visually, this is seen as the light sheet becoming thin and bright as one approaches the focus, and expanding and dimming outwards on either side as one moves away from the focus. This creates a series of images of the light sheet moving along the camera sensor. The setup is shown in Figure 3.13. The Gaussian profile of the light sheet near the illumination objective, and closer to the glass cover slip shows the presence of side lobes. These are seen in Figure 3.13 **D.** highlighted by the blue box. The cause of these side lobes is due to the fact that the light is passing through multiple refractive indices before being measured on camera. As such, experiments should not be done near these lobes as they can cause fluorescence in and out of focus planes.

The beam profile along every cut is fit with a Gaussian function:

$$I_{LS} = I_0 \cdot \exp\left(-2\frac{(y-y_0)^2}{\omega_0^2}\right) \tag{3.8}$$

The beam $1/e^2$ half width is plotted as a function of position as shown in Figure 3.14. In Figure 3.14, the $1/e^2$ axial PSF radius is fit with Equation 3.1 with and without a linear offset, as indicated in the legend, and the beam maximum intensity is fit with a Gaussian and Lorentzian. It is interesting to note that the linear offset leads to a better fitting function, however, the resulting ω_0 obtained from this fit cannot be directly read out as it is mixed with this linear offset. The intensity profile was fitted with a Lorentzian due to the fact that models exist that describe the long axis intensity distributions of confocal volumes with a Lorentzian (Rigler et al. 1993). The Lorentzian fit is shown to better approximate the intensity along the light sheet direction of propagation (x direction) than the Gaussian.

The value at the thinnest part of the light sheet $\approx 2.4\mu m$. The FOV, which is twice the Rayleigh range $2 \cdot x_R = 37.6\,\mu m$. In performing this calibration, one must be careful about laser power as an improper setting can do two things: damage the sensor if its too high ($\geq 5mW$) and saturate the signal preventing a good recording of the beam intensity as a function of position.

Comparing the values from the approixmations in Equation 3.4 to the ones obtained by experiment, the experimental value for the $1/e^2$ beam waist radius, 2.4 μm is 50 % larger than the theoretical value of 1.6 μm. The experimental value for the Rayleigh range, x_R, 37 μm is 70 % larger than the theoretical value of 21.85 μm. These errors can be attributed to the fact that the light sheet profile determined from the scan is non-symmetrical. Because of this, the Rayleigh range appears smaller for values up to 65 on the x-axis, and larger for values greater than 65. This can be a result of

misaligned optics, including but not limited to, improper beam expansion, underfilling the back aperture of the illumination objective, and misalignment of the light sheet with the detection objective. These issues can be alleviated by higher precision control over optical component placement, using motorized control. This is discussed in IV.

3.6.2 Measuring the molecular detection efficiency

This section will provide information that is critical in fitting the ACFs obtained from our SPIM-FCS. As mentioned in Part I, Chapter 2, one of the fitting parameters in the ACF is ω_z, which is the $1/e^2$ half width radius of the PSF along the z-axis. This protocol will help in approximating ω_z so it can be used for fitting.

The molecular detection efficiency (MDE) is a direct representation of the excitation profile of the optical setup. To measure this, 100 nm fluorescent beads (FluoSpheres^{TM} Carboxylate-Modified Microspheres, 0.1 μm, yellow-green fluorescent (505/515), Thermofisher) are embedded in a transparent gel called Gelrite (G1101.0100, Duchefa Biochemie) by mixing 10 mL of deionized water at 90°, 0.125 g of Gelrite, 0.25 mL of 10% $MgSO_4$ salt solution in water, and once the solution has cooled to 40° , by adding 62.5 μL of 100 times diluted manufacturer bead solution. The mixing can be done by intermittently heating up the Gelrite and water in the microwave at 5 second intervals then adding the $MgSO_4$ solution once the Gelrite has completely dissolved (a clear transparent solution) to facilitate the gelling process. Note that the $MgSO_4$ must be at 50° temperature before adding to the heated Gelrite solution. Adding cold $MgSO_4$ solution to the warm Gelrite solution will cause local cooling and gelling leading to an inhomogeneous gel mixture. The beads need to be added before the mixture has completely cooled.

Miniature syringes are created by inserting rubber insulated electrical wire into a capillary that has an outer diameter of 2.5 mm so that it can be held by the sterotaxic

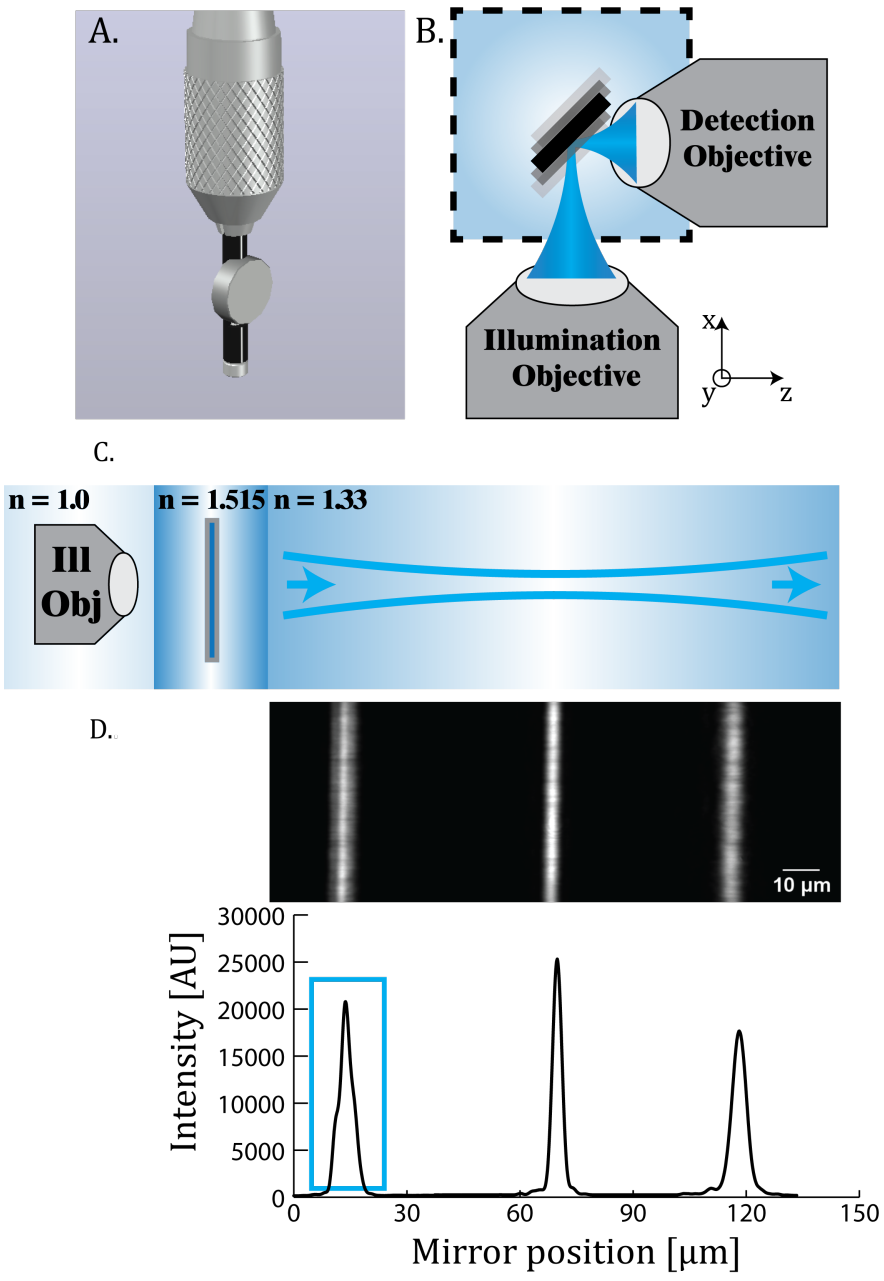

FIGURE 3.13: **A.** Custom made mirror holder for a 7 mm protected silver mirror (PF03-03-P01, Thorlabs) that is held by the stereotaxic cannula holder.**B.** The mirror, denoted by the black bar, is moved along the x axis using the piezo nanopositioner so that the cross section of the light sheet at different points along the x-axis is projected onto the camera sensor. **C.** The path through different refractive indices the light sheet takes.**D.** A representative slice of the light sheet and the Gaussian intensity profile of the slice. The blue box highlights the side lobes which are a result of the changing refractive indices the light path interacts with.

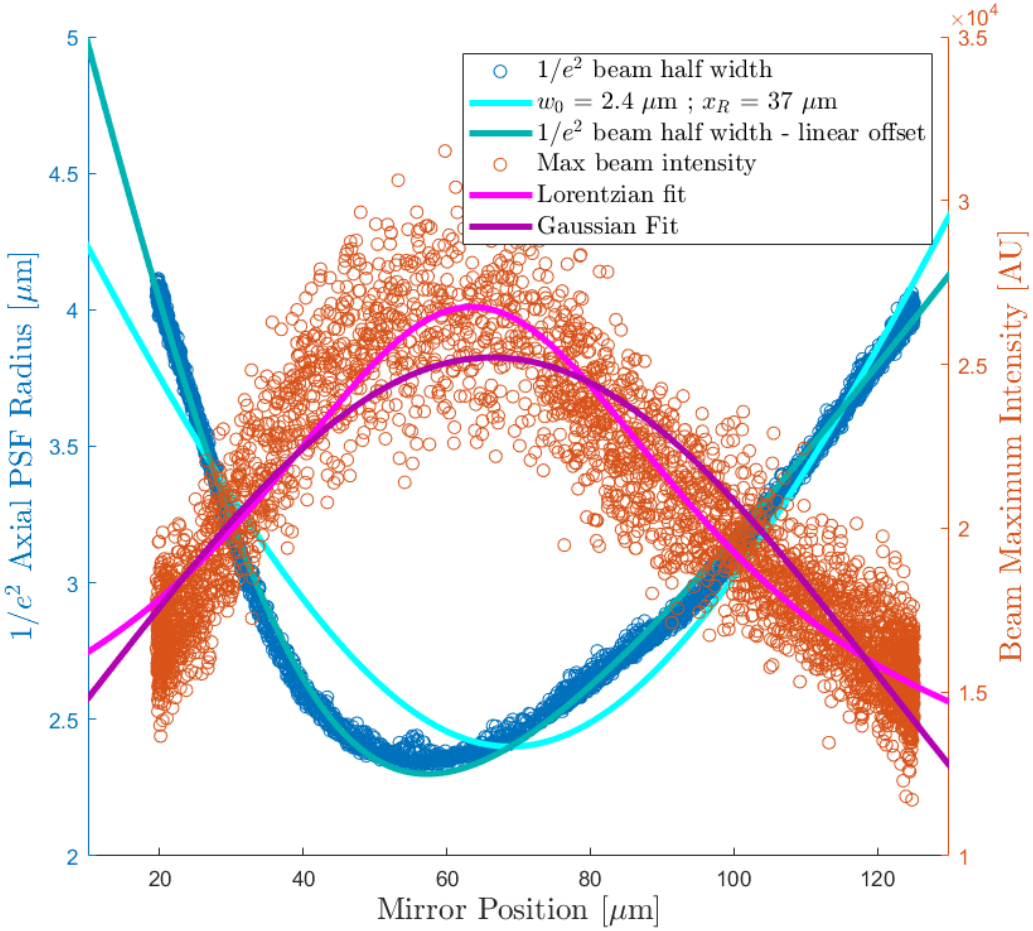

FIGURE 3.14: The blue curve plotted on the left axis is the $1/e^2$ half width as a function of position, and the orange curve plotted on the right axis is the beam maximum intensity as a function of position.

cannula holder. The capillaries are cut by using a diamond knife. Using this miniature syringe, the liquid gel mixture with the beads is syringed into the capillary by pulling on the electrical wire. This is then placed into a 4° fridge to cool and solidify for 5 minutes.

Once the mixture has gelled, a centimeter of the gel is pushed out of the miniature syringes by pushing on the electrical wire. The gel is then rigid and should not bend due to gravity. The excess wire is then cut and the capillary is inserted into the sterotaxic cannula holder. This is then placed in the sample chamber and positioned at the thinnest part (focus) of the light sheet. The beads are scanned along the detection z-axis. This then provides a series of images as the gelled beads are moved in steps of 50 nm through the light sheet.

Using the Beadscan Evaluation plugin on QuickFit3, the image stack of the beads is evaluated by finding beads in the field of view ($\approx$ 100 x 100 pixels) and fitting them with a three dimensional Gaussian. This provide a Gaussian fit to the bead intensity along the three main axes (x,y, and z). The result in the z-direction is another measure of the thickness of the lightsheet which will be important in fitting autocorrelation functions later on.

The following plot shows the values of the averaged Gaussian fits of the axial PSF (determined by the thickness of the light sheet) over multiple days. For my setup the average axial PSF, was $w_z = 2500 \pm 300nm$. If we compare this to the thinnest part of the light sheet, which is the minimum of Figure 3.14, which is 2.3-2.4 μm, we see that they both are in agreement within error.

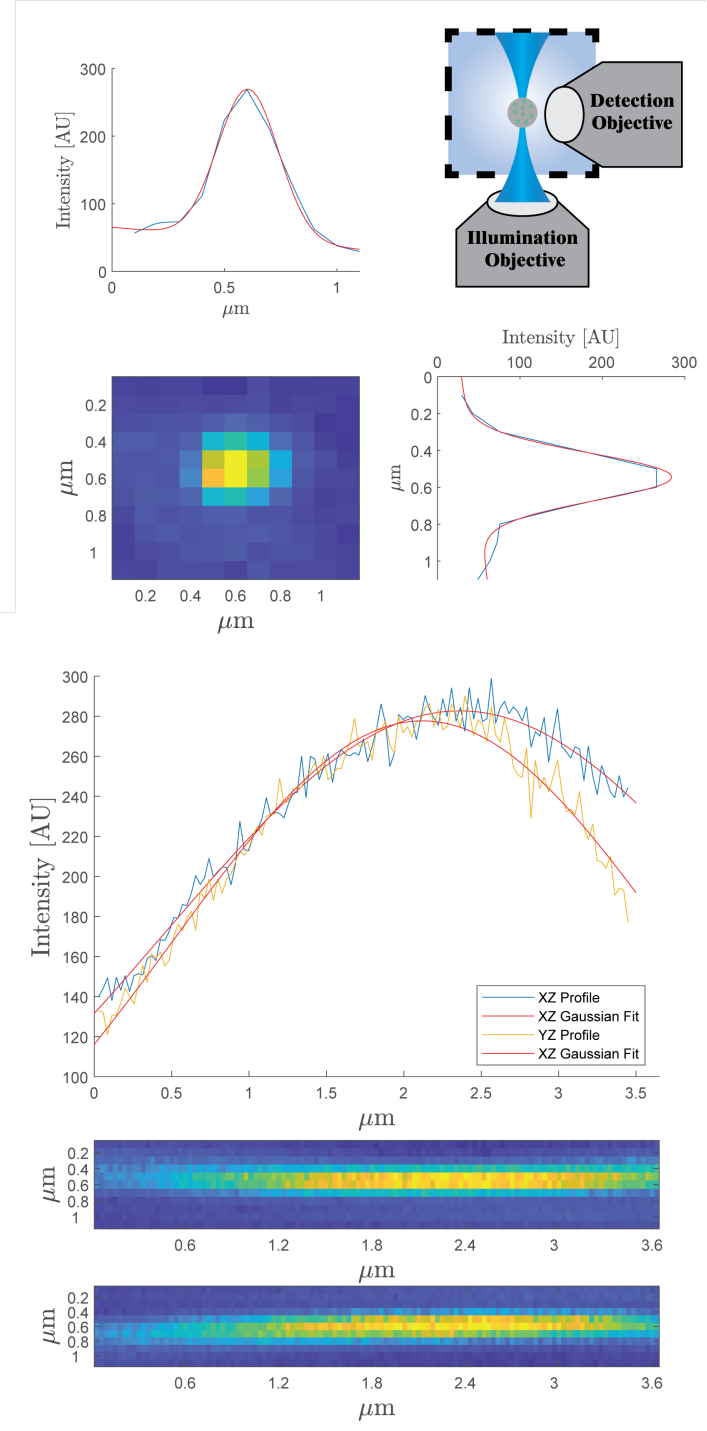

FIGURE 3.15: Image of a representative fluorescent bead shown with Gaussian fits in all planes (xy, xz, yz). For this particular bead, we find: $w_{xy} = 358$ nm , $w_{xz} = 2100$ nm , $w_{yz} = 2240$ nm.

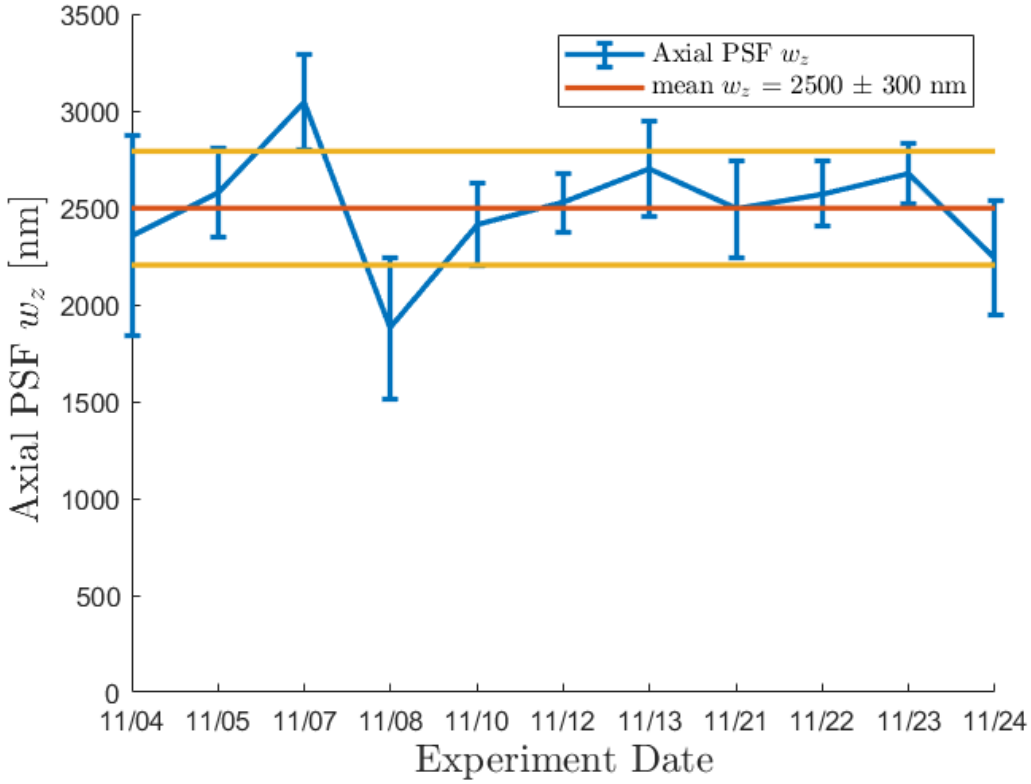

Figure 3.16: The axial PSF measured over multiple days. The error on each day was calculated as the standard deviation of the values obtained for multiple beads visible in the scan.

Part III

SPIM-FCS: Results

Chapter 4

Characterizing Bead Diffusion in Solution

This chapter will discuss the capabilities of the SPIM instrument to perform imaging FCS which was tested using well characterized fluorescent beads. I will begin by describing the steps taken before (sample stability) and after (post processing of data) image acquisition to obtain the best possible ACFs from our SPIM-FCS. I will continue by describing the calibration method used to determine the full PSF (ie. measure its radii both in the axial and lateral directions), which is needed to interpret the result of imaging FCS experiments. I will then discuss the microscope's ability to determine absolute diffusion coefficients and concentrations of beads in aqueous solutions, which is compared to confocal FCS measurements.

4.1 Post processing of raw data

4.1.1 Segmenting the intensity trace

Before I discuss fitting the ACF's obtained from different samples, it should be noted that there are certain treatments that are done to the intensity trace of each pixel when calculating the ACF to alleviate effects of photobleaching and sample drift. The intensity

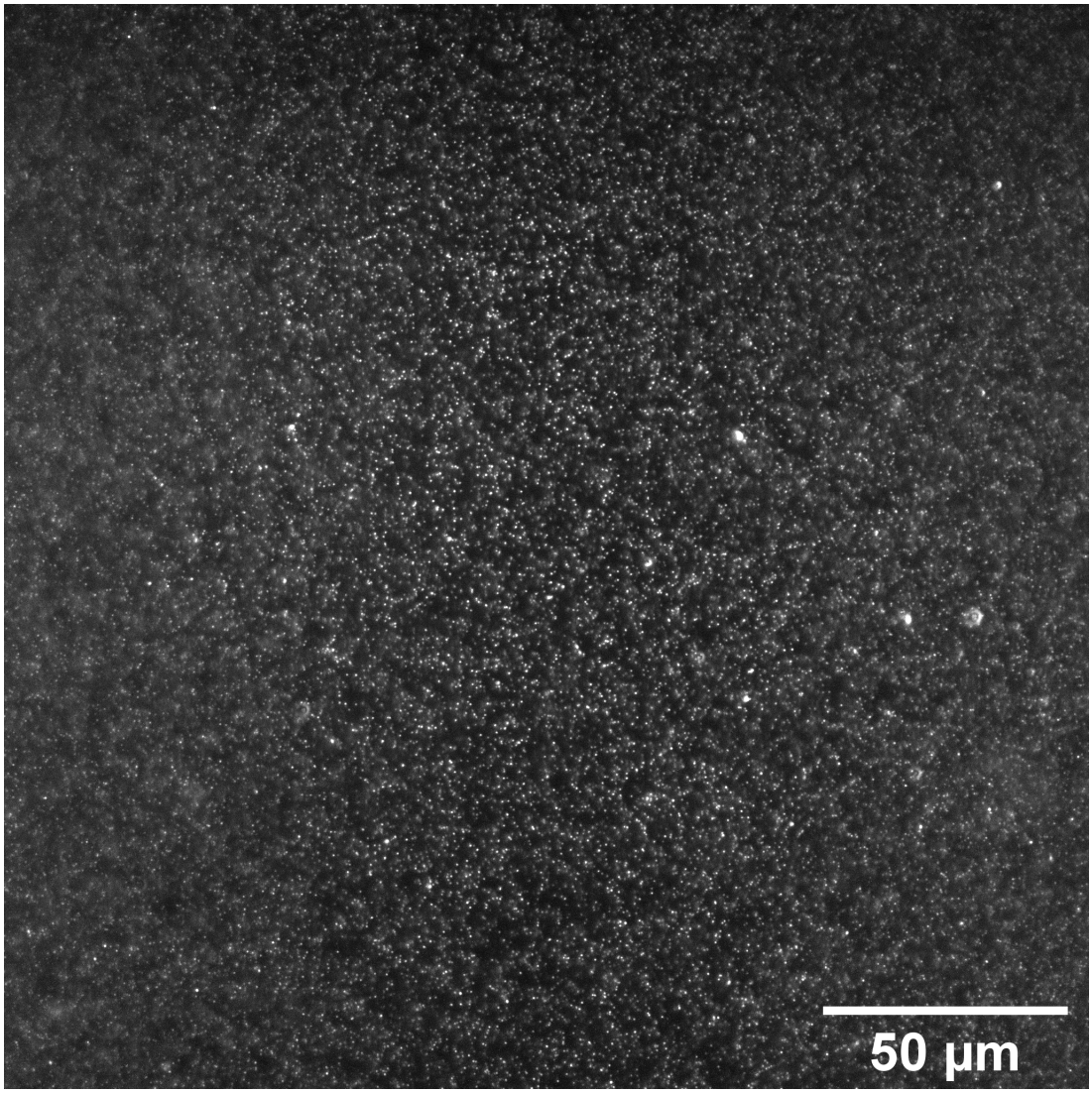

Figure 4.1: A SPIM image of a 100 nm bead solution with a concentration of 4 nM held in a FEP sample bag. Note the focus of the light sheet where there is the greatest contrast between the beads and the background yielding the clearest image. This is where data for ACFs was gathered.

trace can be divided into several user defined time segments, where each segment is auto correlated, and then all ACFs are averaged to produce the final ACF. This is seen in Figure 4.2, for a measurement with a decreasing average intensity and for a measurement with a steady average intensity. Segmenting the trace has a weaker influence when the intensity trace fluctuates evenly about the average over time. This is because the measurement is consistently self similar over short and large time scales.

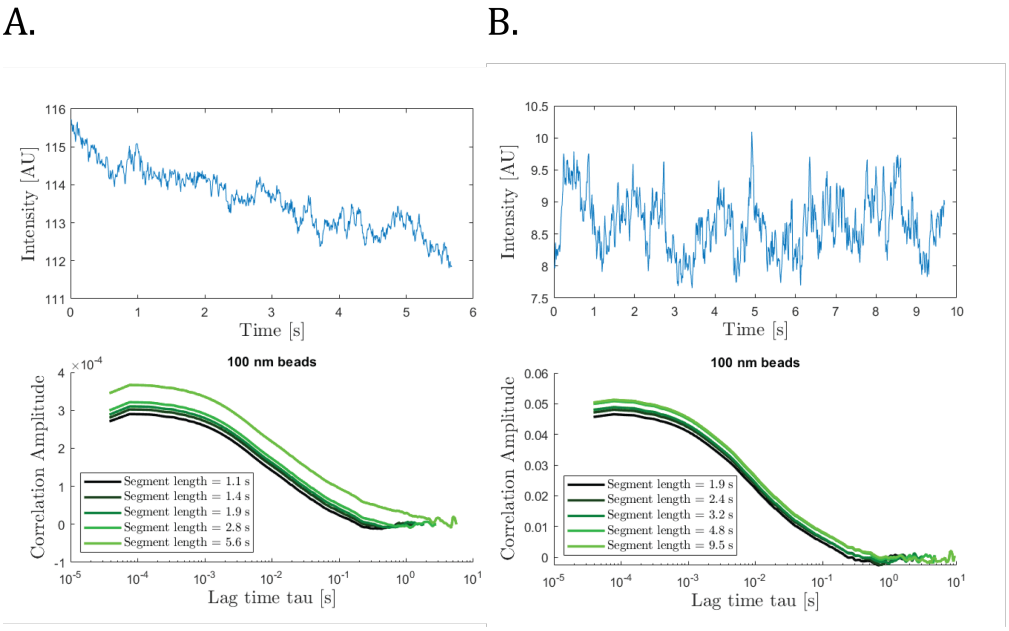

FIGURE 4.2: Both time traces are generated with a 100 nm bead sample at 4 nM. **A.** The panel shows a sample with a decreasing average intensity over time. Note that when fewer segments are used, the ACF shifts further to the right, leading to a slower diffusion measurement, and lower concentration measurement. This sample is not background corrected. **B.** This panel shows a sample with an average intensity that fluctuates uniformly around its mean value. Segmenting the time trace has very little influence on the calculated ACF.

4.1.2 Background noise and after pulsing

Uncorrelated background noise strongly affects the amplitude of the ACF (Rigler et al. 1993), therefore background noise must be estimated and subtracted, if not, an overestimation of the concentration could result. There is lots of noise that is attributed

to the camera. This is accounted for by taking approximately 5000 images in the same ROI and same acquisition speed as the actual sample but with the laser off, as electron noise is dependent on these factors. Background correction is performed by subtracting the average background series from the fluorescent image stack. This is shown in Figure 4.3. Background subtraction changes the correlation amplitude by a factor of 100, but does not influence the correlation decay time, so the diffusion coefficient can be retrieved either way. This high background is caused by the increased noise in camera read out when operating at high frame rates (25 kFPS).

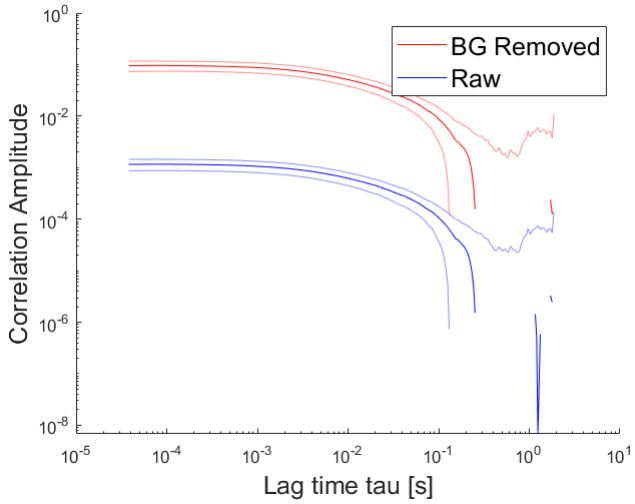

FIGURE 4.3: Generated with a 100 nm bead bead sample at 4 nM. ACF shown with no background removal, and background removal.

In addition to background subtraction, there is an effect that camera sensor exhibits known as afterpulsing. This is a release of electrons from ambient photons when the camera starts up after a previous acquisition. This is largely noticeable at early lag times of ACF's as seen in Figure 4.4. Furthermore, a known issue with Hamamatsu sensor readout (from a private call with Hamamatsu engineers) is that the first and last row of pixels appear brighter when reading at a high frame rate ($\geq$ 5000FPS). The first and last row should be cropped out before calculating the autocorrelation functions.

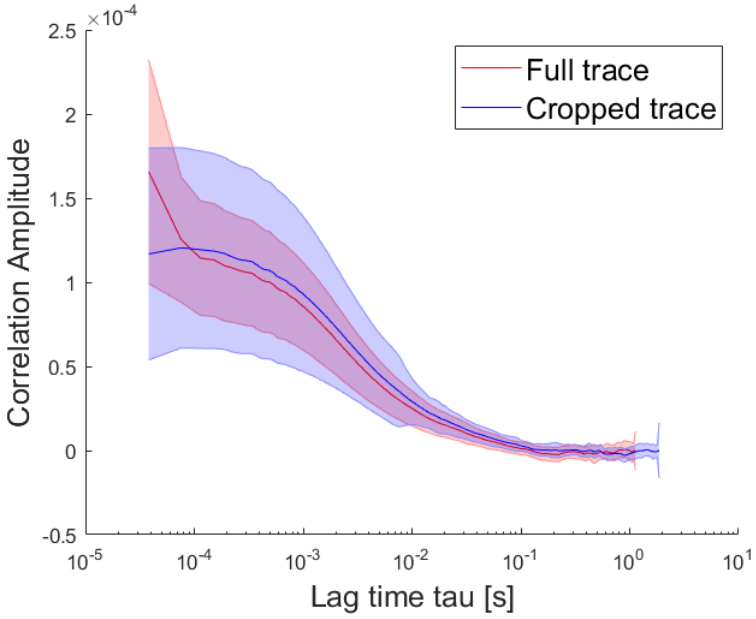

FIGURE 4.4: ACF calculated for the signal measured from a 100 nm bead sample at 4 nM. Removal of the first few frames where the camera shows after pulsing removes the upward spike seen at early lag times.

4.1.3 Environment vibrations and sample stability

Keeping all aspects of the experimental setup vibration free is crucial when performing imaging FCS. Vibrations from the environment can have adverse effects the ACF and the calibration process. Figure 4.5 shows oscillations in the 10^{-2} s lag time range which can limit the accuracy of a fitting function. Furthermore, the bead scan calibration requires a stable setup as single beads must be imaged, and the slightest of motions can extend the apparent PSF, leading to an incorrect fitting function. Vibrations can be minimized by floating the optical table on which the microscope is installed.

4.2 Determining the lateral PSF radius, w_{xy}

The lateral PSF radius, w_{xy} is crucial in determining the diffusion coefficients and concentrations of samples. To obtain the best and most accurate FCS results, the thinnest

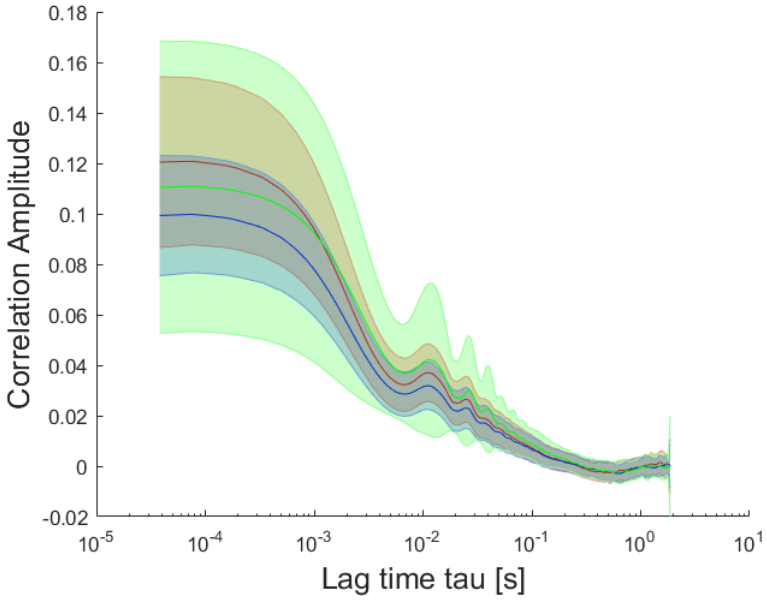

Figure 4.5: Multiple ACF acquired for 100 nm bead solutions without a floating optical table overlayed and displaying oscillations in the ACF due to mechanical vibrations of the experimental setup.

part of the light sheet must coincide with the imaging plane of the detection objective, and since this alignment can change daily, determination of the full PSF must be performed each day before an experiment.

The fitting models described in Chapter 2 depend on the MDE of the microscope, which in turn is dependent on the pixel size a in the image plane, and PSF widths in the axial and lateral planes, w_z and w_{xy} respectively, as the MDE is a convolution of the PSF and the shape of the pixel [Chapter 2, Equation 2.6]. The pixel size a in the object plane is dependent on camera manufacturing, the magnification used, and the eventual binning of the signal by binning adjacent pixels, a is given by the ratio of the nominal pixel size (6.5 μm for our camera) and the magnification (60X, for our detection objective), yielding 108 nm per pixel for our setup in the absence of binning. The height of the PSF, w_z can be directly determined from the fit of the 3D image of beads as shown in the previous chapter where the average value over multiple days was

$\omega_z = 2500 \pm 300/, \text{nm}$. The average value obtained from the Gaussian fit of the image of many different beads is used in the subsequent fitting of the ACF. This value straight forwardly obtained from the bead scan can be used because w_z is minimally influenced by the pixel size. On the contrary, the lateral MDE is heavily dependent on the pixel size and the bead scan yields the MDE, instead of the PSF in the lateral plane. To determine this factor, an imaging FCS calibration is used, as explained below.

This calibration is performed by using beads in aqueous solution, held in a Teflon-FEP bag (Fluorinated ethylene propylene, 50A (12.7 μm) Teflon® FEP Film, American Durafilm) with a refractive index of 1.341–1.347 making it virtually invisible in water (refractive index of 1.33). The bag is created by folding a small FEP sheet in half, and heat sealing (Tabletop Impulse Sealer - 12", ULINE) 0.5 cm away from the folded edge. This creates a hollow sheath, which is then sealed at one end (Figure 4.6 A.). The bead solution (F8803, Invitrogen) is pipetted into the open end, which is then heat sealed to create a small bag that is roughly 5 mm by 5 mm in dimensions (Figure 4.6 B.) which contain approximately 50 μL of solution. These bags are held by a clamp that inserts into the sterotaxic cannula holder (Figure 4.6 C.). The light sheet interacts with the regions of the bag that doesn't have any heat sealing (the right hand side of the bag in Figure 4.6 C). which prevents unnecessary light scattering. For this calibration, 100x dilution was performed on the manufacturer bead stock solution, resulting in a concentration of 4 nM.

Ultimately, the PSF width w_{xy} is determined by fitting the ACF from bead solutions while fixing w_z (obtained from the bead scan), and the value of the bead's diffusion coefficient, D_{ref}.

Typically, in confocal FCS when such a calibration of the instrument is performed, a reference for the diffusing species (typically a well characterized dye such as eg. Alexa-488 or Fluorescein) is obtained from the literature. However, in SPIM-FCS, this D_{ref}

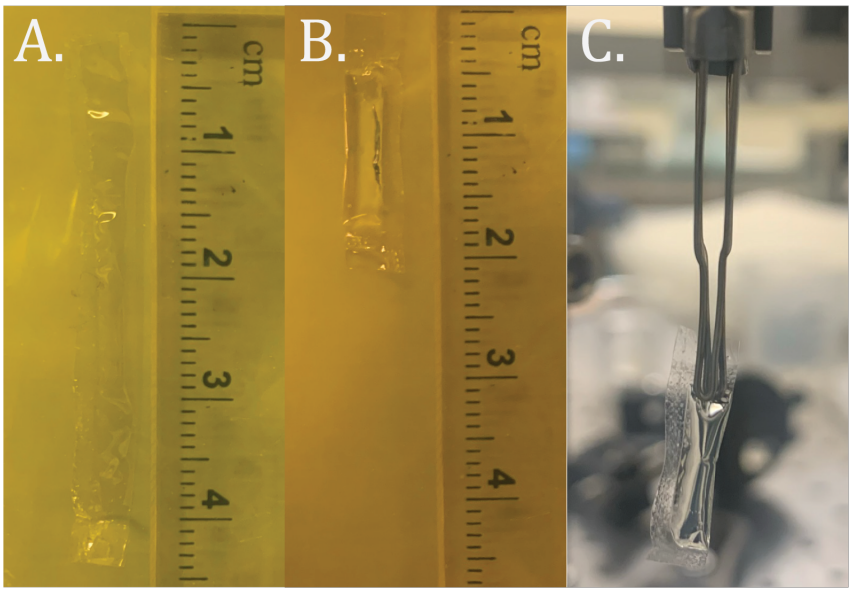

FIGURE 4.6: FEP bag used to hold samples in solution for SPIM-FCS measurements. A larger bag is illustrated here for clarity.

can be determined experimentally using the exact same calibration sample as long as the pixel dimensions are known, since they can be used as a ruler. The method by which w_{xy} is determined is as follows and is known as the pixel-binning methods first established by Bag et al. 2012 for TIRF-FCS, and refined by Singh et al. 2013 for SPIM-FCS.

SPIM-FCS models from Section 2 will still hold if the signals coming from several adjacent pixels in a square region are binned together, as long as the pixel value a is replaced by $b \cdot a$, where b represents the binning factor. If $b \cdot a$ is much larger than the unknown w_{xy}, the fitting models dependence on w_{xy} becomes weak, and as such, in the case of large pixel size (or binning), the particle dwell time is only dependent on the known pixel size. In the limit where $a >> \omega_{xy}$, the diffusion coefficient D can be obtained without any knowledge of w_{xy}. This is shown in Figure 2.2, as with larger binning, resulting in a larger pixel size a, the Gaussian PSF becomes dominated by the quadratic nature of the pixel. This value of D is what we call the reference diffusion coefficient, D_{ref}. Once this is obtained, the value of D can be fixed in the fitting model

(Equation 2.34), and the ACF obtained in the case where there is no binning ($b = 1$), can be fit for w_{xy}, which yields the true w_{xy}.

Because the limit $a >> \omega_{xy}$ is difficult to reach even at high binning, the data is analyzed using a series of bin sized and a number of different queries for ω_{xy}. When performing the fitting of the ACFs to obtain D_{ref}, the unknown PSF width w_{xy} is fixed to different test values that are distributed around the expected value ($\omega_{xy} \approx \lambda/2\mathrm{NA}_{det}$). So if we expected $w_{xy} = 500$ nm, we would choose $w_{xy} = 100, 300, 500, 700, 900$ nm. It is important to note here that sufficient binning must be performed such that the convergence of the diffusion coefficients can be observed. To achieve the convergence of the diffusion coefficients, higher binning is required, and so a ROI of 100 by 100 pixels was chosen to perform a maximum binning of 20 by 20 pixels. This leads to a binned pixel size of about 2200 by 2200 nm^2. This is shown in Figure 4.7, where the convergence is clearly seen.

The diffusion coefficient of the beads, D_{ref} is then fixed by taking the average of the diffusion coefficients determined at the highest binning (here, $D_{ref} = 4.7\mu m^2/s$ at 20×20 binning), ACFs are fit again for different bin sizes using the known values of D_{ref} and ω_z to return the values of w_{xy}, which is shown in Figure 4.8. The true w_{xy} is chosen as the value obtained $b = 1$ where the measurement is more reliable (which is 550 ± 80 nm here).

This calibration is performed each day before experiments, Figure 4.9 shows the lateral PSF w_{xy} obtained over multiple days.

Using these calibration methods, we can then determine the absolute diffusion coefficients and concentrations of our samples (without binning). The ω_{xy} is stable over multiple days without fluctuating largely, however, even the smallest variations can change the diffusion coefficient that is calculated from ACF. When comparing this value to the

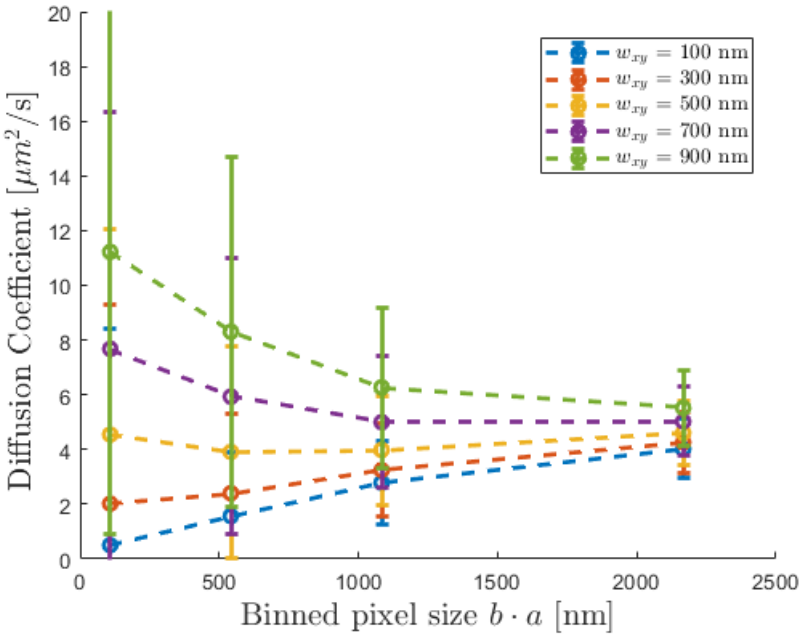

FIGURE 4.7: Plot of the diffusion coefficient D obtained by changing the binning value for multiple test w_{xy} using a larger ROI of 100 by 100 pixels, and a maximum binning of 20 by 20. D_{ref} is determined by taking the average of the diffusion coefficients determined at the highest binning (here, $D_{ref} = 4.7\mu m^2/s$ at 20×20 binning).

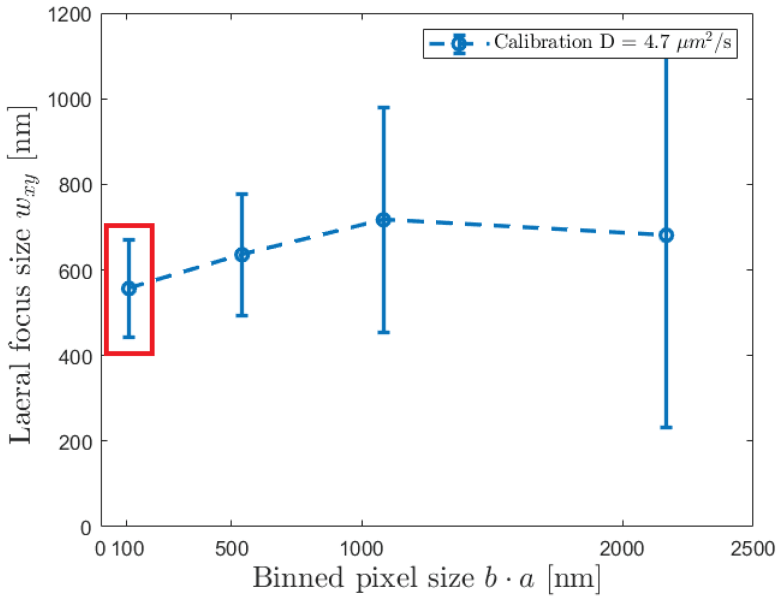

FIGURE 4.8: Binned ACF fitted for w_{xy} while keeping D_{ref} and ω_z fixed for different pixel $b \cdot a$ sizes. The sample used was Invitrogen 100 nm FlurorSpheres, with $w_z = 2500 \pm 100nm$ and $a = 108.3nm$. The true w_{xy} is the lateral focus size obtained at $b = 1$ highlighted by the red box, which is 550 ± 80 nm.

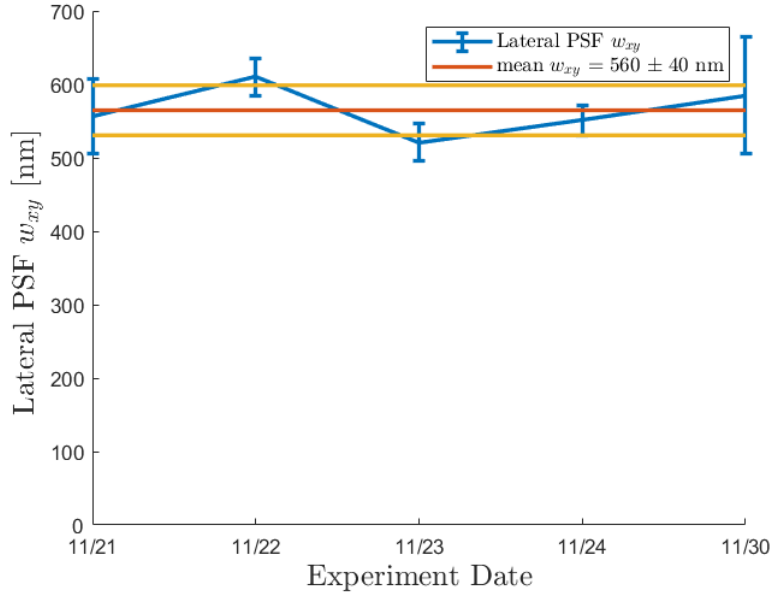

FIGURE 4.9: Fit result for w_{xy} for different days.

theoretical estimate, $\omega_{xy} \approx \lambda/2\text{NA}_{det}$, with $\lambda \approx 520$ nm and $\text{NA}_{ill} = 1$, $\omega_{xy} \approx 260nm$. The observed ω_{xy} is almost twice as large, however, work done by Singh et al. 2013 and Wolfgang Krieger 2014 show that their measured values for ω_{xy} lie between 400 and 650 nm, so our setup lands well within that range. This calibration method relies entirely upon the quality of the sample, here it is the 100 nm beads. Beads have a tendency to aggregate and these aggregations lead to an increased spread of diffusion coefficients as larger objects will diffuse slower. A lower D_{ref} results in an underestimation of ω_{xy}, which in turn results in lower measured diffusion coefficients and a higher concentration.

4.3 Absolute diffusion coefficients and concentrations

Using the calibration method above, measurements were carried out on 100 nm beads solutions of varying concentrations (a well characterized system where we expect simple diffusion), and corroborated with measurements done on a confocal FCS. A comparison of the ACF obtained from these two instruments is shown in Figure 4.10. Note that the decay of the confocal ACF is at earlier times as the width of the confocal excitation volume was 296 nm which is approximately half that of the SPIM.

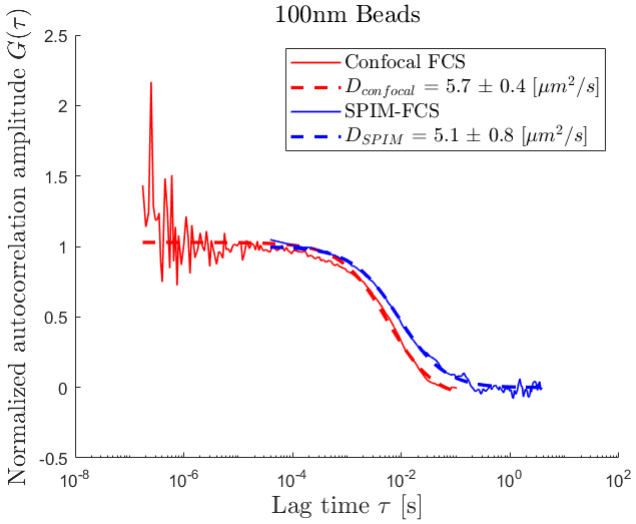

FIGURE 4.10: Normalized ACF obtained from my SPIM-FCS and a confocal FCS for 100 nm bead solution at 4 nM.

4.3.1 Confocal vs. SPIM FCS concentration

Using the same confocal measurements, an exact value for the concentration can be determined for the varying concentrated bead samples used. From this, a calibration curve showing the comparison of concentrations measured through SPIM-FCS, and the ones measured for the diluted samples in confocal FCS can be observed in Figure 4.11. This shows that within error, SPIM-FCS can determine the concentration of samples,

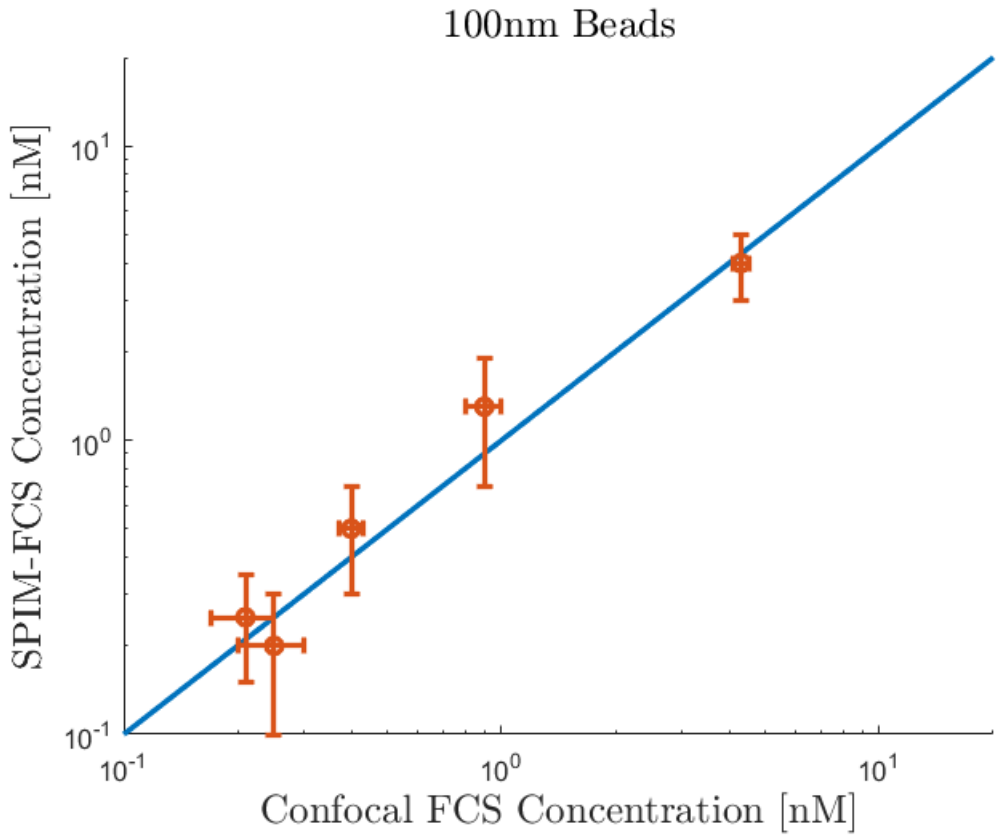

FIGURE 4.11: Concentration measurements from confocal FCS and SPIM-FCS of multiple 100 nm bead samples at varying concentrations.

In knowing the concentration, we can show the effect of dilution on the measured diffusion coefficients and concentrations. Figure 4.12 compares the diffusion coefficient measured from a confocal FCS compared to our SPIM-FCS. In Figure 4.12, one can see that the lower the concentration, the larger the error in estimating the diffusion

coefficient due to the lower signal in both instruments. They both agree within error, which can be accounted for by the estimation of the confocal parameter in the confocal FCS and the lateral and axial PSF in our SPIM-FCS. However, with the combined data displayed in Figure 4.11 and Figure 4.12, our home built SPIM-FCS can accurately determine concentrations and absolute diffusion coefficients.

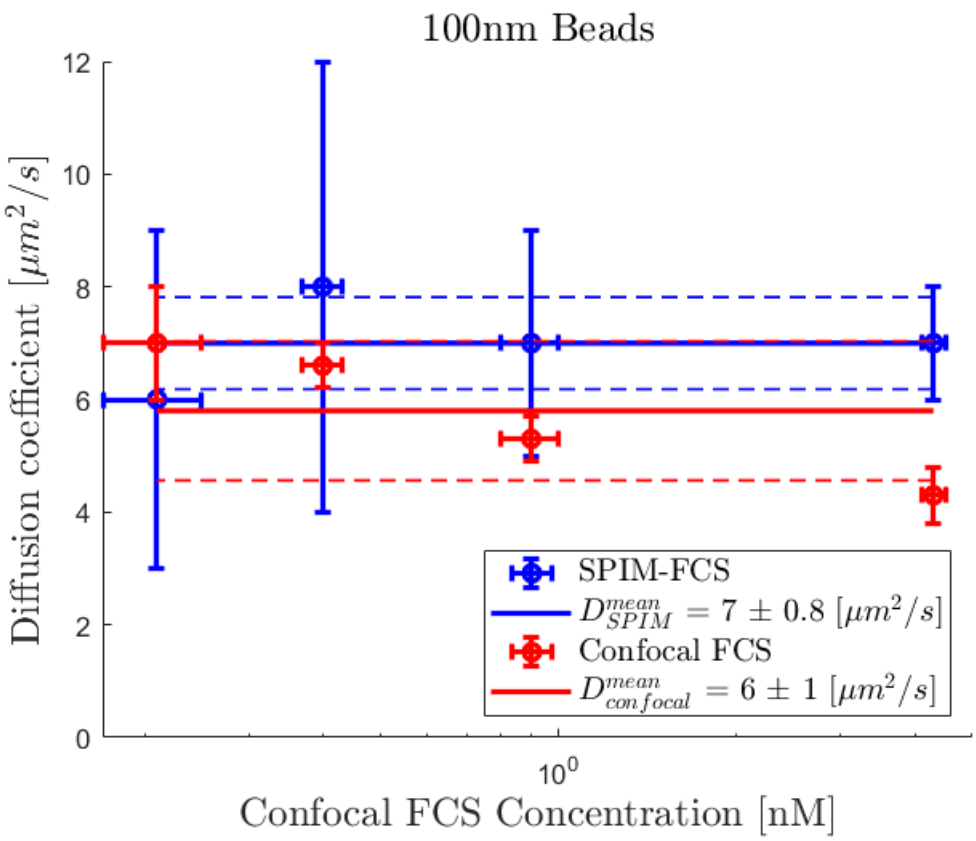

FIGURE 4.12: Absolute diffusion coefficient measurements from confocal FCS and SPIM-FCS of multiple 100 nm bead samples at varying concentrations.

For each of these concentrations, the counts per particle (CPP) was extracted and plotted as a histogram as a function of concentration. This is shown in Figure 4.13. Comparing these values obtained to the CPP from a confocal FCS instrument, shown in Figure 4.14, we can see that there is a factor 4-5 between the two. The laser power was kept constant for both concentration series (80 nW for confocal, and 6.5 mW for

SPIM-FCS). These Figures imply that the SPIM-FCS can be operated at a lower laser power, and still yield adequate ACFs.

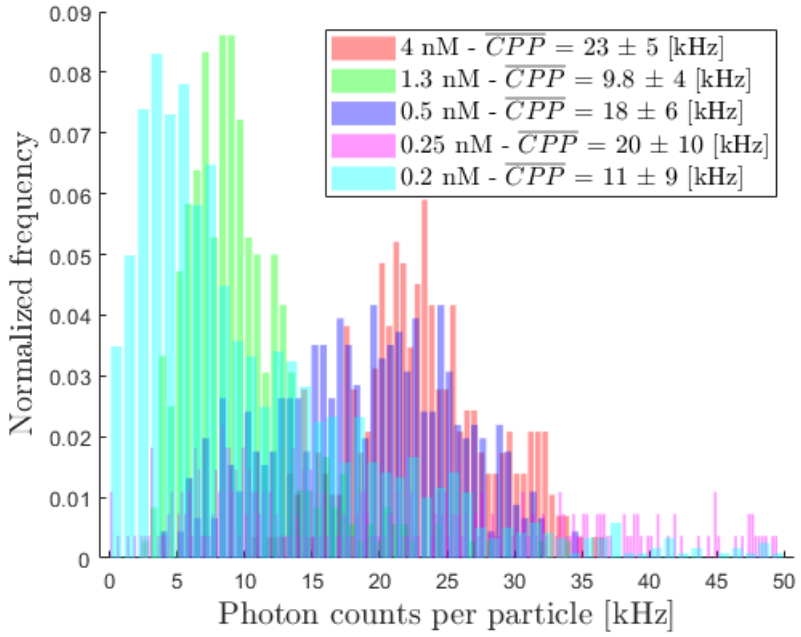

FIGURE 4.13: CPP for 100 nm beads in solution at varying concentrations using the SPIM-FCS. The lower the concentration, the larger the spread in the CPP due to he dilute solution.

4.4 Measurements across the light sheet

Different areas of the light sheet have a different thickness. This thickness leads to larger areas of the sample to fluoresce creating out of focus noise. The following experiment was done to show this effect. This is shown in Figure 4.15.

An ROI of 2048 x 6 was taken, and split up into 8 pieces of 256 x 6. Each of these 8 pieces was fit to determine the diffusion coefficient and particle number shown in Figure 4.16 and Figure 4.17 respectively. Both show a dependence on the position over the light sheet, as well as possibly position in the FEP bag. The changing thickness illuminates larger regions which increases the out of focus light which would increase the measured

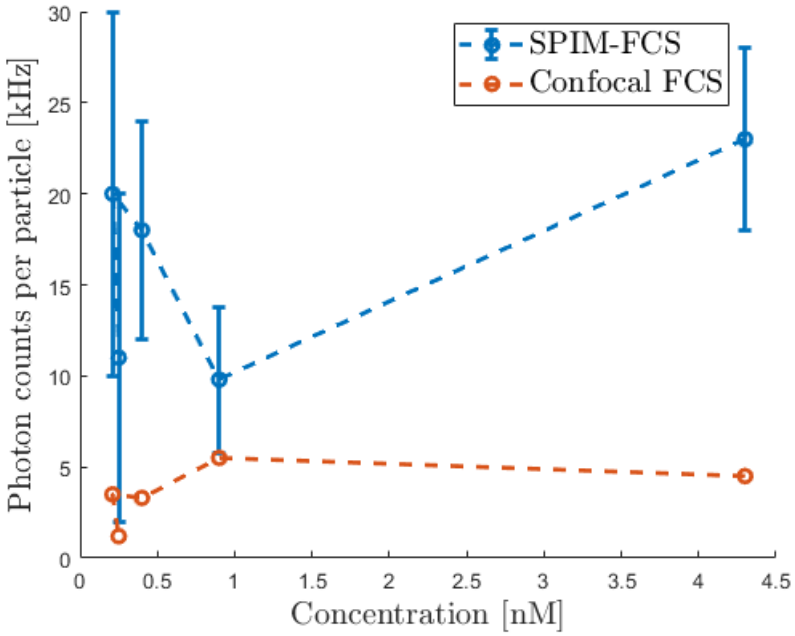

FIGURE 4.14: CPP for 100 nm bead in solution at varying concentrations for confocal FCS and SPIM-FCS.

particle number around the focus which is at 100 - 150 μm.The decrease in diffusion coefficient would be a result of the fact that the fitting parameters for w_{xy} and w_z are not uniform across the light sheet, and as such the resulting diffusion coefficient would also not be the same.

As previously done, I can extract the CPP for the varying position along the light sheet. THis is shown in Figure 4.18. What is clearly observed is that as the intensity peaks where the light sheet is the thinnest, the CPP increases proportionately, and then decay to either side of the peak. This validates the idea that a high CPP is obtained where there is low background, which is a result of being in the thinnest region of the light sheet. In this region, we get the most accurate results in terms of diffusion and concentration.

In the following Figure 4.19, I show the comparison of two differently sized fluorescent

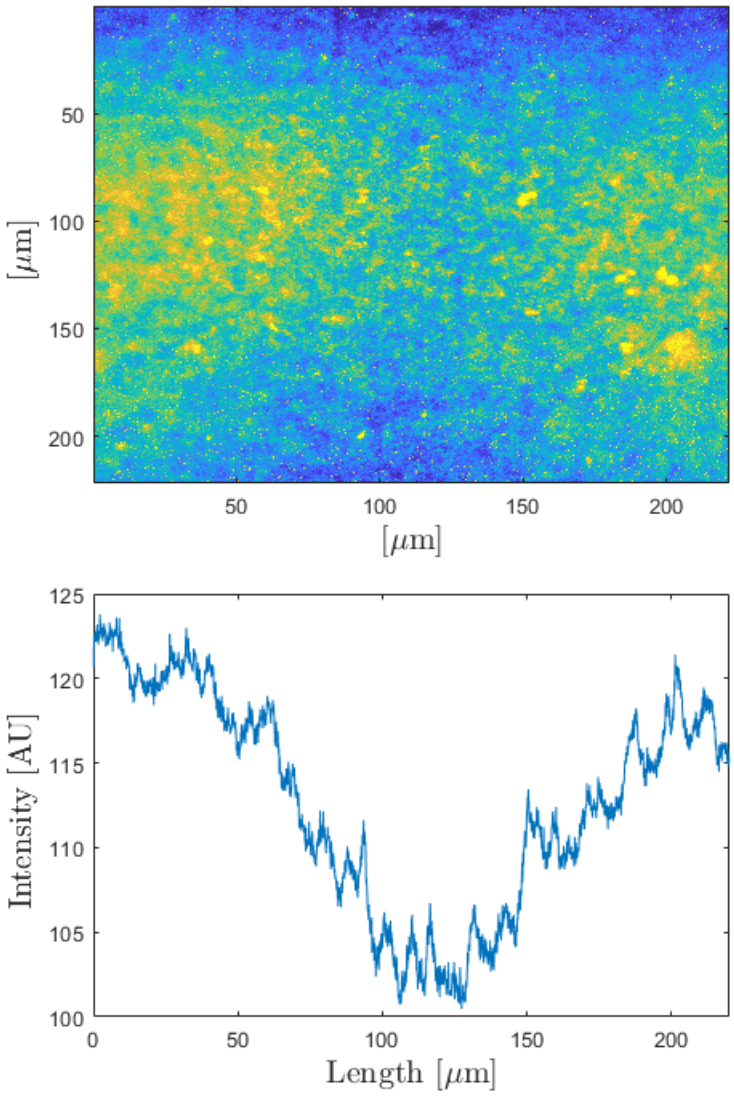

Figure 4.15: The top figure shows the average intensity over multiple frames across the full FOV of the camera. The bottom figure is the corresponding intensity profile along the x direction. Where the intensity is the lowest corresponds to the thinnest part of the light sheet.

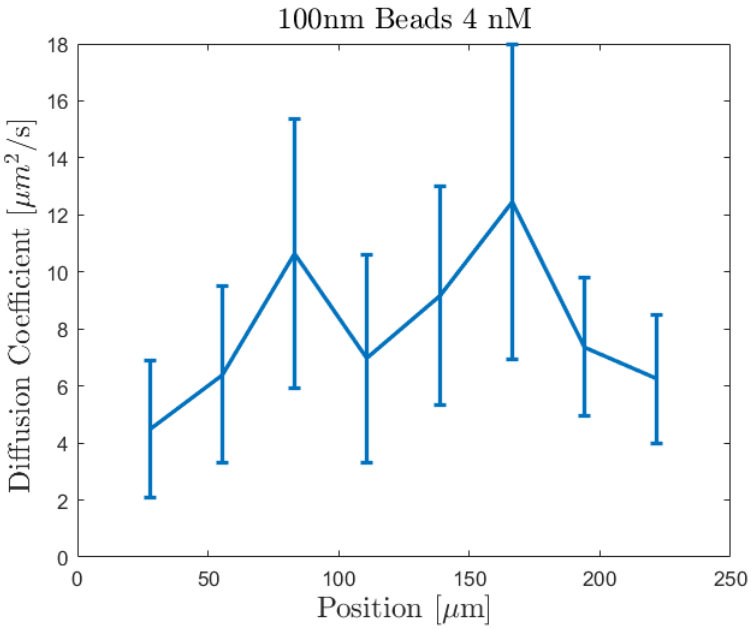

FIGURE 4.16: The diffusion coefficient calculated over a length of 250 μm

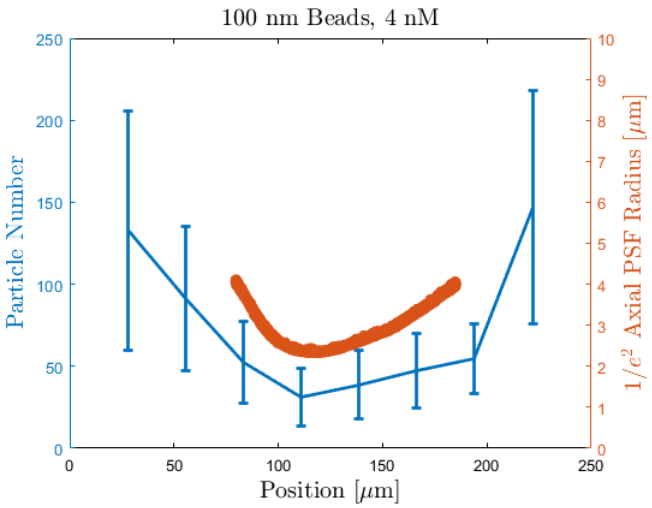

FIGURE 4.17: The particle number calculated over a length of 250 μm superimposed with the thickness of the light sheet at the given position.

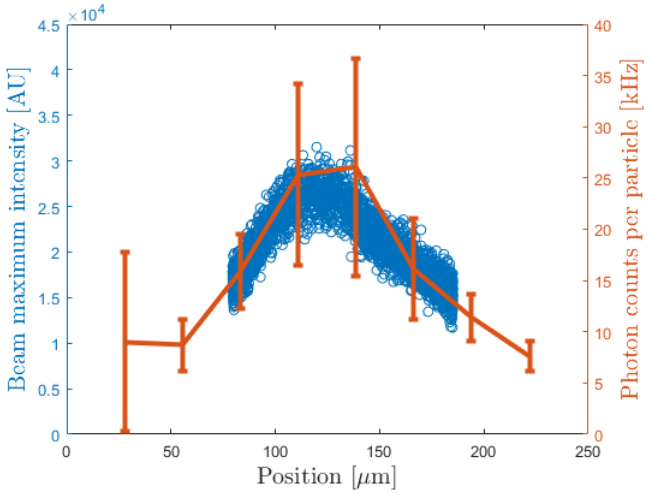

FIGURE 4.18: The left axis shows the beam intensity as a function of position, and the right axis shows the CPP of the 100 nm bead sample at varying positions in the light sheet.

beads, one 40 nm, and the other 100 nm. Both have a similar excitation/emission profile. The 40 nm beads are estimated to be twice as fast as the 100 nm beads and that is shown in the ACF fits as the 100 nm beads have an average diffusion coefficient of 5 ± 1 $\mu m^2/s$ where as the 40 nm beads have an average diffusion coefficient of 12 ± 2 $\mu m^2/s$. However, due to the age of the 40 nm beads, the larger error on the fit can be a result of aggregations and reduced fluorescence making some beads have a poor emission rate.

Extracting the CPP for both bead sizes, 100 nm and 40 nm, shown in Figure 4.20, it can be seen that the CPP for the 40 nm beads is roughly 10 times smaller than the 100 nm beads. This can be attributed to two factors, sample geometry, and sample age. The 100 nm beads have a greater volume than the 40 nm beads by a factor of ≈ 16. This means that there is more fluorescent volume in the larger beads accounting for the higher CPP. Secondly, the 40 nm bead sample is much older than the 100 nm beads. This can result in a loss of fluorescence due to decay which would result in a lower CPP. The relative ratio of the CPP validates the instruments ability to accurately capture the differences between geometrically varying samples through the CPP. Thus, the CPP can

be used as an indicator for the correct positioning in the light sheet.

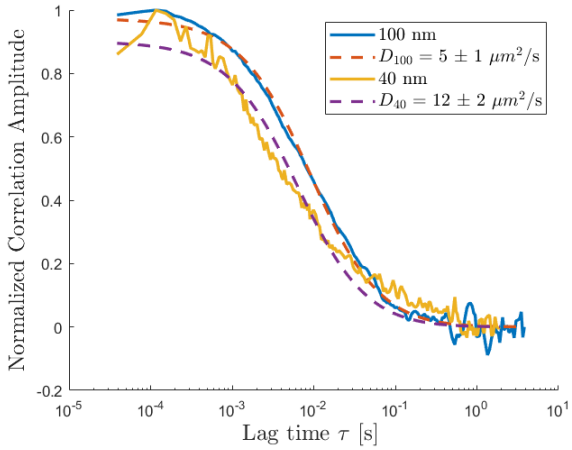

FIGURE 4.19: Representative curves of 40 nm and 100 nm diameter fluorescent beads. The error comes from the standard deviation of 1500 curves. What is clear is that the 40 nm beads are twice as fast as the 100 nm beads which is expected from the dependence of the Stokes-Einstein relationship on the hydrodynamic radius.

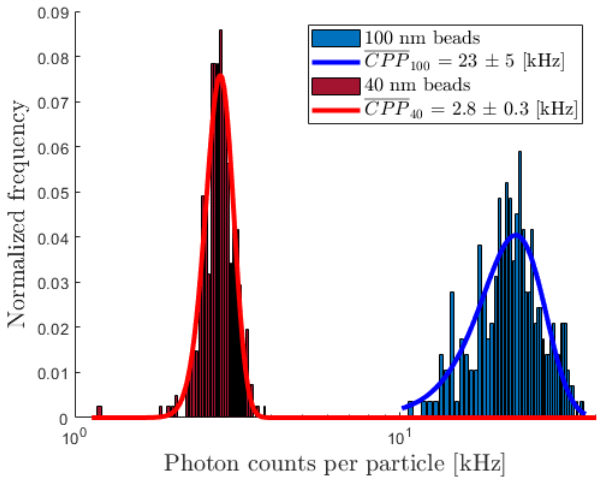

FIGURE 4.20: Representative curves of the CPP of 40 nm and 100 nm diameter fluorescent beads.

Chapter 5

Imaging nuclei in *D. melanogaster* using SPIM

This chapter will discuss the capabilities of the SPIM instrument to perform imaging. The samples used were *Drosophila melanogaster* embyros, where the protein Bicoid was labelled with eGFP. Samples were graciously prepared by Lili Zhang.

Embryos were collected 4 hours after egg laying on agarose embryo collection plates, dechorionated by hand, and mounted on capillaries (OD 2.5 mm) using heptane-dissolved glue (Perez-Romera et al. 2018). The capilarries were inserted into the the sterotaxic cannular holder for imaging.

Figure 5.1 shows a series of images where the embryo, once in focus, was moved through the light sheet using the piezo stage. Each image in the montage is separated by 50 nm. Figure 5.2 shows a crop of just the nuclei, demonstrating the ability to be resolve them from the background of the embryo through the intensity profile plotted.

Due to the complex nature of the embryo, and that the nuclei and the embryonic cytoplasm have different refractive indices, we see structural artifacts known as stripe artifacts (Wolfgang Krieger 2014, Capoulade et al. 2011). There are characteristic of

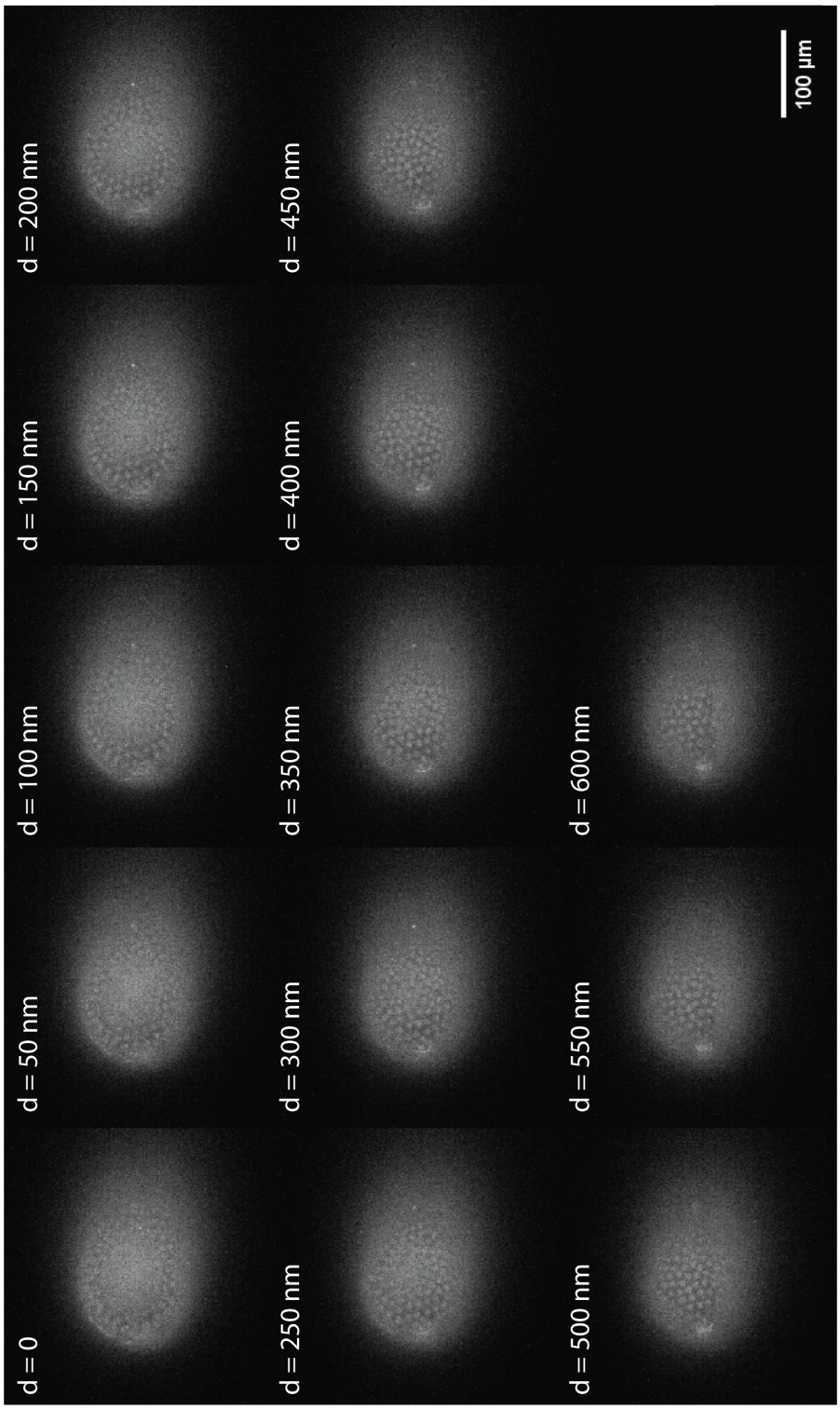

Figure 5.1: Montage of a series of images of BCD-eGFP expressing *D. Melanogaster* embryo at nuclear cycle 12. This was taken by moving the sample along the z direction through the light sheet bringing different plane of the sample into focus. The step size was 50 nm. Background subtraction was performed by turning of the excitation laser source and recording a 500 frames and subtracting the average frame from the z stack of embryo images.

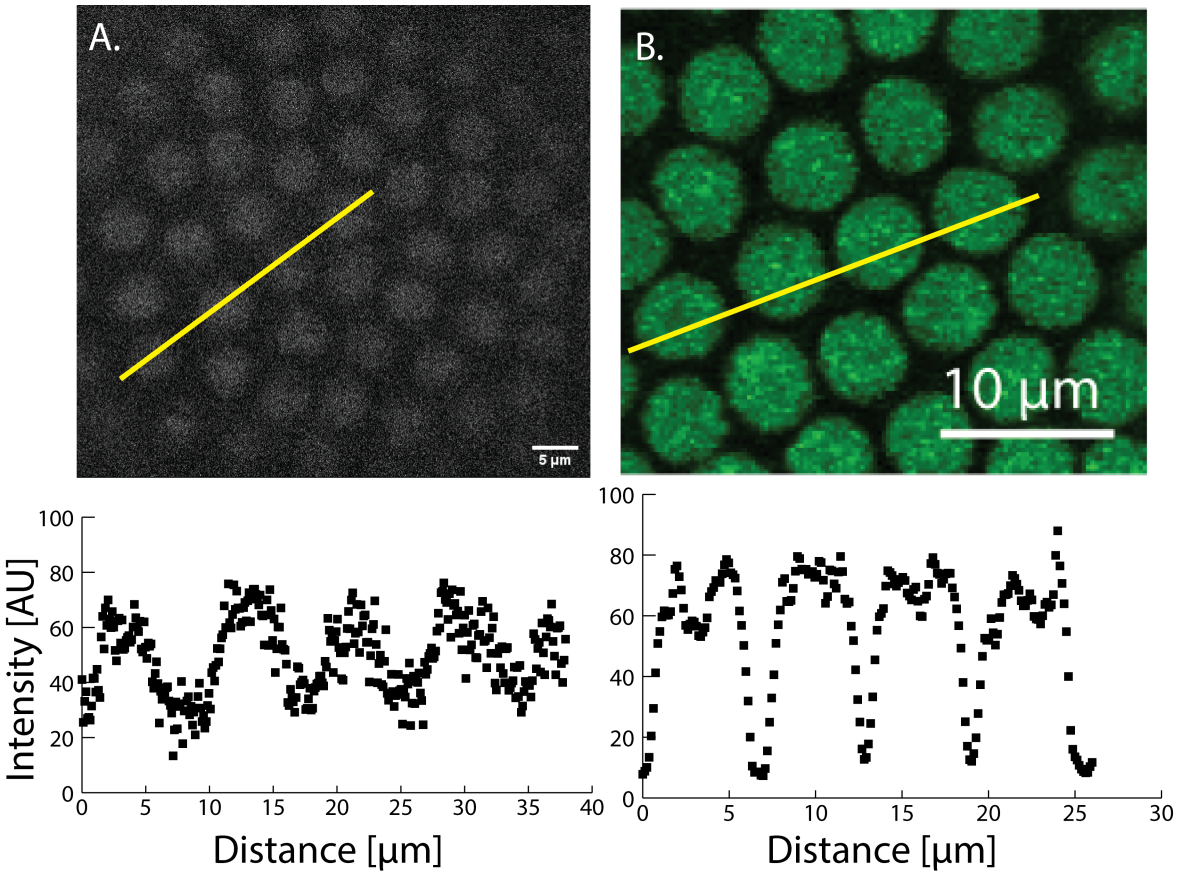

FIGURE 5.2: Nuclei of a BCD-eGFP expressing *D. Melanogaster* embryo at nuclear cycle 12. **A.**The yellow line indicates a line intensity profile which is plotted in the graph as a function of position. Background subtraction was performed by turning of the excitation laser source and recording a 500 frames and subtracting the average frame from the z stack of embryo images. **B.** Shows *D. Melanogaster* embryo at nuclear cycle 12 captured with a confocal microscope by Lili Zhang.The yellow line indicates a line intensity profile which is plotted in the graph as a function of position. Note the significant difference in resolution, however, the imaging ability of the SPIM is satisfactory.

casting long streaks along the direction of light sheet propagation, as seen in Figure 5.3 on the left hand side. Areas with these artifacts should be avoided in SPIM-FCS experiments as it would influence the measured diffusion and concentration values. Figure 5.3 shows the worst case scenario to display the effect of stripe artifacts, however, which proper positioning of the sample, the sample can be seen without these artifacts (Figure 5.2).

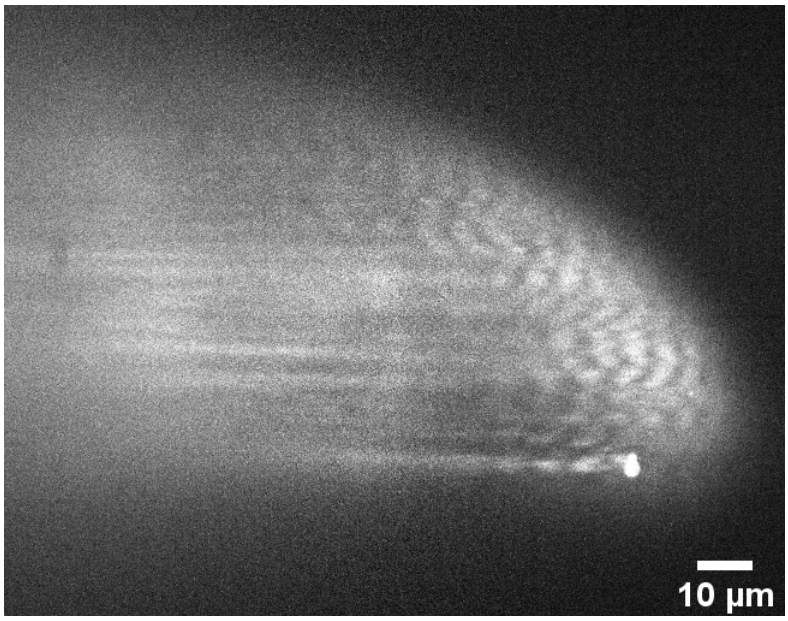

FIGURE 5.3: Stripe artifacts in BCD-eGFP expressing *D. Melanogaster* embryo.

The SPIM instrument built can not only be used for imaging FCS measurements but for its imaging capabilities as well. Although it is not intended for that purpose, it can accurately distinguish between complexes in heterogeneous environments such as the embryo. With some work and time, the SPIM instrument can be used to perform imaging FCS on these complex systems.

Part IV

Conclusion

Chapter 6

Conclusion

Over the course of my Master's thesis, I was motivated by the complex environment of fruit fly embryos and the dynamic molecular processes that dictate their fate. In order to accurately estimate the diffusion of proteins on the molecular level in a heterogeneous system, I needed to build a microscope which would allow spatial mapping of the diffusion coefficients and concentrations. Our group is very skilled at single point FCS, but we wanted to take it further by exploring imaging FCS by way of SPIM, and how it could be used to study the embryo.

I began by thoughtfully planning each aspect of the SPIM-FCS as specific requirements must be met for accurate diffusion and concentration measurements. The first step was to create a water tight, insulating, and non-corrosive sample chamber. The accuracy of the build was crucial as the detection objective would be imbedded in the sample chamber. Knowing that the sample would need to be brought into focus, and taking inspiration from inverted light microscopes, I decided to embed the detection objective in the chamber, which allowed me to bring the light sheet into the focal plane of the detection objective by moving the entire chamber (together with the embedded detection objective) along the detection and illumination axes. The light sheet itself was created by beam shaping a supercontinuum laser source that allowed me to fluorescently

excite my samples with a range of wavelengths centered around the peak excitation of the fluorophores. The beam was created into a light sheet using a cylindrical lens, and then focused using a low NA air objective. The thickness was characterized by building a sample holder which would allow for nanometer resolution using a piezo stage. This resulted in a $1/e^2$ half width of the PSF in the axial direction of $\omega_z = 2500 \pm 300$ nm, close to the predicted theoretical thickness. The detection pathway consisted of the chamber embedded water dipping high NA objective, where the light was focused onto a fast sCMOS camera. The PSF in the lateral direction was determined by using calibration samples of 100 nm fluorescent beads, in combination with pixel binning. This showed that the lateral radius of the PSF was $\omega_{xy} = 560 \pm 40$ nm, close to the expected value. By determining these values for my setup, I was able to perform imaging FCS measurements on bead samples, where dynamics are very well characterized.

In the course of a year and a half, I was able to plan and build a SPIM-FCS that is able to accurately determine the absolute diffusion coefficients and concentrations of fluorescent beads ranging from 0.1 nM to 4 nM. The results were corroborated by taking single point FCS measurements on the same samples.

With a single point FCS, only a single point measurement can be made at one time. So each curve takes the length of the experiment time, say 30 seconds. In SPIM-FCS, we can multiplex this process such that each pixel acts as a confocal volume. I was able to obtain upwards of 10000 ACF curves at one time over a span of 30 seconds. If I wanted to take the same amount of curves in single point FCS, I would be experimenting for 3 days! However, there is always a drawback to multiplexing through camera based sensors. The camera I used allowed a temporal resolution of 38 μs, whereas many single point detectors can reach a resolution in the nanoseconds. This means that certain fast photophysics effects are inaccessible to SPIM-FCS.

6.1 System modifications

Although the SPIM-FCS instrument I have built can do the job, there are always ways to improve. I will split this discussion up into the different aspects of the SPIM-FCS: the illumination arm, the sample chamber, and detection arm.

The supercontinuum laser source is a great tool as it can excite using many wavelengths simultaneously. Work done by Rouger et al. 2016 show a SPIM that has the illumination arm where the laser is directed by a fibre optic cable to the cylindrical lens, and the beam expanders, cylindrical lens, and illumination objective are coupled and mounted on a piezo stage. This would allow extremely fine positioning of the light sheet into the focal plane of the detection objective. Another possibility, which has its own drawbacks, is using a water dipping illumination objective. An objective by Thorlabs, TL20X-MPL, has a thin shape which would allow it to be placed orthogonal and very close to a high NA objective (generally larger in size). In having a water dipping objective, the NA would be twice that of the one currently in use, meaning a thinner light sheet resulting in less background fluorescence. However, manufacturing issues can come into play where the slightest offset can be detrimental in terms of focus alignment as these optics would be fixed into the sample chamber.

As for the sample chamber, temperature dependent experiments would be fantastic to run, especially for biological systems such as the fly embryo. I believe this can be done by using heating elements attached to the sample chamber which would heat up the solution inside. This would open up a host of other experiments that can be done, and easily characterized by looking at beads since the Stokes Einstein relationship can be used as a comparison. Related to the sample chamber, the sample holder can be updated by having motorized control over all axes which would greatly improve precision and repeatability. The sample chamber is currently on two coupled linear stages that both have a translational resolution of 10 μm. The $1/e^2$ half width of the light sheet is 2.5

μm. This means that even the smallest possible movement of the detection objective along the axial direction will move it out of focus, so even when the alignment is good, it may not be the best.

The detection pathway is dominated by the detection objective and the camera. A larger NA detection objective would always be preferred as more light can be collected, and more structures laterally resolved. The camera in use is arguably one of the best on the market currently. Some aspects of the camera were not exploited during this thesis. The noise of the camera is dependent on how cooled the sensor is (Hamamatsu Photonics K.K. 2018). The lower the temperature, the better the SNR. The sCMOS in use has a water cooling feature that was not used but would be extremely beneficial in the case of noisy systems such as the fly embryo, as water cooling to -30° reduces the dark current by a factor of 10 (currently air cooled to -10°). Furthermore, I would love to test out an EMCCD on this SPIM-FCS to see the effect of having a larger pixel size (EMCCD usually has a pixel size of 24 μm) on signal detection for low light systems.

6.2 Concluding remarks

I believe that many upgrades can be made to this SPIM-FCS as it has a very open plan and every aspect of it can be altered. This system is also a great learning tool to teach how concepts in biophysics such as image formation, fluorescence, and diffusion work because nothing is hidden behind a black box as is the case with most commercial microscopes.

Bibliography

Abu-Arish, A., Porcher, A., Czerwonka, A., Dostatni, N., and Fradin, C. (2010). High mobility of bicoid captured by fluorescence correlation spectroscopy: Implication for the rapid establishment of its gradient. *Biophysical Journal* 99(4), 33–35. ISSN: 15420086.

Bag, N., Sankaran, J., Paul, A., Kraut, R. S., and Wohland, T. (Aug. 2012). Calibration and limits of camera-based fluorescence correlation spectroscopy: A supported lipid bilayer study. *ChemPhysChem* 13(11), 2784–2794. ISSN: 14397641.

Born, M. and Wolf, E. (1999). *Principles of Optics: Electromagnetic Theory of Propagation, Interference and Diffraction of Light.*

Brown, R. (1828). XXVII. A brief account of microscopical observations made in the months of June, July and August 1827, on the particles contained in the pollen of plants; and on the general existence of active molecules in organic and inorganic bodies. *The Philosophical Magazine* 4(21), 161–173. ISSN: 1941-5850.

Capoulade, J., Wachsmuth, M., Hufnagel, L., and Knop, M. (2011). Quantitative fluorescence imaging of protein diffusion and interaction in living cells. *Nature Biotechnology* 29(9), 835–839. ISSN: 10870156.

Chakraborty, T. and Apalkov, V. M. (2003). Quantum cascade transitions in nanostructures. *Advances in Physics* 52(5), 455–521. ISSN: 00018732.

Digman, M. A. and Gratton, E. (2009). Analysis of diffusion and binding in cells using the RICS approach. *Microsc Res Tech* 72(4), 323–332.

Einstein, a. (1905). Uber d4e von der rnolekuZarh%net4schem Theorie der WUrme geforderte Bewegumg vow in ruhenden P Z ikss4ykeitem. *Ann. d. Phys.* 322(8), 549–560.

Gupta, V. P. (2016). *Principles and Applications of Quantum Chemistry*. ISBN: 9780128034781.

Hamamatsu Photonics K.K. (2018). ORCA-Flash4.0 V3 Digital CMOS Camera C13440-20CU / C13440-20CU01. (August), 1–96.

Hansen, J. P. and McDonald, I. R. (2006). Theory of Simple Liquids. *Theory of Simple Liquids* (November).

Höfling, F. and Franosch, T. (2013). Anomalous transport in the crowded world of biological cells. *Reports on Progress in Physics* 76(4), 1–55. ISSN: 00344885.

Hopkins, P., Fortini, A., Archer, A. J., and Schmidt, M. (2010). The van Hove distribution function for Brownian hard spheres: Dynamical test particle theory and computer simulations for bulk dynamics. *Journal of Chemical Physics* 133(22). ISSN: 00219606.

Korzh, S., Pan, X., Garcia-Lecea, M., Winata, C. L., Pan, X., Wohland, T., Korzh, V., and Gong, Z. (2008). Requirement of vasculogenesis and blood circulation in late stages of liver growth in zebrafish. *BMC Developmental Biology* 8, 1–15. ISSN: 1471213X.

Krichevsky, O. and Bonnet, G. (2002). *Fluorescence correlation spectroscopy : the technique*. Vol. 65, 251–297.

Lakowicz, J. R. (2006). *Principles of Fluorescence Spectroscopy*. Vol. Third Edit. ISBN: 9780387312781.

Lasser, T. and Hassler, K. (2005). Single molecule detection and fluorescence correlation spectroscopy on surfaces. (January).

Manzo, C. and Garcia-Parajo, M. F. (2015). A review of progress in single particle tracking: From methods to biophysical insights. *Reports on Progress in Physics* 78(12). ISSN: 00344885.

Orme, N., M, R., and Phillips, R. (2016). Cell biology by the numbers. *Choice Reviews Online* 53(10), 53–4367. ISSN: 0009-4978.

Pedrotti, F. L. and Pedrotti, L. S. (1993). *Introduction to Optics*.

Perez-Romera, C. A., Tran, H., Coppey, M., Walczak, A. M., Fradin, C., and Dostatni, N. (2018). *Live Imaging of mRNA Transcription in Drosophila Embryos*, Chapter 10. ISBN: 9781493987719.

Perrin, J. (1910). Mouvement brownien et molécules. *Journal de Physique Théorique et Appliquée* 9(1), 5–39. ISSN: 0368-3893.

Rigler, R., Mets, U., Widengren, J., and Kask, P. (1993). Fluorescence correlation spectroscopy with high count rate and low background: analysis of translational diffusion. *European Biophysics Journal* 22(3), 169–175. ISSN: 01757571.

Rouger, V., Alchini, R., Kazarine, A., Gopal, A. A., Girouard, M.-P., Fournier, A. E., and Wiseman, P. W. (2016). Low-cost multimodal light sheet microscopy for optically cleared tissues and living specimens. *Journal of Biomedical Optics* 21(12), 1. ISSN: 1083-3668.

Shimomura, O. (1979). Structure of the chromophore of Aequorea green fluorescent protein. *FEBS Letters* 104(2), 220–222. ISSN: 00145793.

Shindy, H. A. (2017). Fundamentals in the chemistry of cyanine dyes: A review. *Dyes and Pigments* 145, 505–513. ISSN: 18733743.

Singh, A. P., Krieger, J. W., Buchholz, J., Charbon, E., Langowski, J., and Wohland, T. (Apr. 2013). The performance of 2D array detectors for light sheet based fluorescence correlation spectroscopy. *Optics Express* 21(7), 8652. ISSN: 1094-4087.

Weiss, M., Hashimoto, H., and Nilsson, T. (2003). Anomalous protein diffusion in living cells as seen by fluorescence correlation spectroscopy. *Biophysical Journal* 84(6), 4043–4052. ISSN: 00063495.

Wohland, T., Shi, X., Sankaran, J., and Stelzer, E. H. (2010). Single Plane Illumination Fluorescence Correlation Spectroscopy (SPIM-FCS) probes inhomogeneous three-dimensional environments. *Optics Express* 18(10), 10627. ISSN: 1094-4087.

Wolfgang Krieger, J. (2014). Mapping Diffusion Properties in Living Cells. (July), 1–277.

Yu, S. R., Burkhardt, M., Nowak, M., Ries, J., Petráek, Z., Scholpp, S., Schwille, P., and Brand, M. (2009). Fgf8 morphogen gradient forms by a source-sink mechanism with freely diffusing molecules. *Nature* 461(7263), 533–536. ISSN: 00280836.

Zimmerman, S. B. and Trach, S. O. (1991). Estimation of macromolecule concentrations and excluded volume effects for the cytoplasm of Escherichia coli. *Journal of Molecular Biology* 222(3), 599–620. ISSN: 00222836.